Metastructure and strain-defect engineered Cu-doped TiO$_x$ coating to enhance antibacterial sonodynamic therapy

Songsong Wang [a,b], Ji Tan [a,**], Haifeng Zhang [a], Shiwei Guan [a], Yibo Zeng [a,b], Xiaoshuang Nie [a,b], Hongqin Zhu [a], Shi Qian [a], Xuanyong Liu [a,b,c,*]

[a] State Key Laboratory of Advanced Ceramics, Shanghai Institute of Ceramics, Chinese Academy of Sciences, Shanghai, 200050, China
[b] Center of Materials Science and Optoelectronics Engineering, University of Chinese Academy of Sciences, Beijing, 100049, China
[c] School of Chemistry and Materials Science, Hangzhou Institute for Advanced Study, University of Chinese Academy of Science, Hangzhou, 310024, China

ABSTRACT

Sonodynamic therapy (SDT) has attracted widespread attention in treatment of implant-associated infections, one of the key factors leading to implant failure. Nevertheless, constructing efficient ultrasound-triggered coatings on implant surfaces remains a challenge. Herein, an acoustic metastructure Cu-doped defective titanium oxide coating (Cu-TiO$_x$) with lattice strain was constructed *in situ* on titanium implant to realize effective sonocatalysis. The redistribution of Cu atoms broke the pristine lattice of TiO$_2$ during the thermal reduction treatment to regulate its energy structure, which favored separation of electron-hole pairs generated by ultrasound radiation to enhance the sonocatalytic generation of reactive oxygen species. In addition, the acoustic metastructure enhanced the absorption of ultrasound by Cu-TiO$_x$ metastructure coating, which further promoted its sonocatalytic effect. Thus, Cu-TiO$_x$ metastructure coating could efficiently eliminate *Staphylococcus aureus* and *Escherichia coli* infections under ultrasonic irradiation in 10 min. Besides, the osteogenic property of implant was significantly improved after infection clearance *in vivo*. This work provides a fresh perspective on the design of SDT biosurfaces based on metastructure and strain-defect engineering.

1. Introduction

Implant-associated infections (IAIs) are a highly threatening challenge in dental implants and orthopedic surgery. In addition to the surgical implantation process, secondary bacterial infections persist throughout the service life of dental implants and bone implants. Prolonged use of antibiotics confers bacterial resistance and immune escape properties, which undoubtedly poses a significant obstacle to the eradication of IAIs [1,2]. So far, the physical removal of IAIs by subsequent surgical procedures or even replacement with dental implants and bone implants has been the main clinical solution. However, traditional debridement methods impose a serious clinical burden on patients and the threaded structure and rough surface of dental implants and bone implants make complete elimination challenging [3,4]. Therefore, it is crucial to explore effective and non-invasive treatment strategies for IAIs. Exogenous stimulus-triggered therapeutic effects could be externally activated by ultrasound (US) [5,6], light [7,8], electrical field [9,10], magnetic field [11], and so on. They allow highly effective, non-invasive and non-antibiotic-dependent treatments without the need for subsequent surgical procedures.

US has great potential for the therapy of deep bone tissue infections due to its non-invasiveness, minor energy attenuation and high tissue penetration [12–14]. Sonodynamic therapy (SDT) is an emerging non-invasive therapeutic approach in which US delivers energy to sonosensitizers to stimulate the separation of electron-hole pairs, triggering redox reactions that ultimately produce lethal reactive oxygen species (ROS, including hydroxyl radicals (·OH), superoxide anions (·O$_2^-$), and singlet oxygen (^{1}O$_2$)) [15–17]. However, the development of sonosensitizers is limited to nanoparticles, which cannot be stabilized at the site of infection for long periods of time, and therefore do not perform US-triggered antibacterial function immediately when bacterial infection occurs. There should be two fundamental factors for

sonosensitizers that overcome IAIs: (1) providing mechanical support and (2) long-term stabilization in the lesion. Hence, the development of efficient US-triggered coatings on implant surfaces seems to be a reasonable approach. Unfortunately, loading nanoscale sonosensitizers on implant surfaces is an ineffective strategy because they typically exhibit limited US absorption efficiency, resulting in unsatisfactory ROS yields. To date, the development of US-triggered coatings that effectively absorb US and enable SDT remains a challenge.

In recent years, the emergence of metamaterials has broken the limitations of traditional materials [18–20]. Notably, acoustic metastructures can control the propagation of US in new ways [21–24]. The rise of metamaterials has created a wave in the biomedical field, and researchers have achieved a series of exciting results [25,26]. Inspired by this, the construction of acoustic metastructure coatings on titanium (Ti) surfaces can enhance US absorption and improve sonocatalytic efficiency. Titanium oxide (TiO_2), a commonly used sonosensitizer, is not only cytocompatible but also easy to achieve *in situ* growth on Ti surfaces [27–29]. Therefore, the development of TiO_2 acoustic metastructure coatings will bring opportunities for SDT. However, the large band gap (~3.2 eV) and fast carrier recombination rate (50 ± 30 ns) of TiO_2 have become the biggest obstacles to its efficient ROS generation [30]. To address these problems, heterostructures and oxygen defect engineering have been employed to suppress electron-hole pairs recombination [31, 32]. In contrast, oxygen defect engineering is a simple and effective option to improve the charge transfer performance of semiconductor sonosensitizers, which significantly improves catalytic performance [33,

34]. Although a variety of sonosensitizers have been developed by this strategy, there is still great room for improvement in their ROS yields to achieve efficient SDT.

Lattice distortion can be introduced by heteroatomic doping and vacancy defects, which will introduce intermediate energy levels in the band gap. Unlike the impurity energy levels caused by individual defects, they are not discretely distributed in the band gap, but are stacked together and connected to the edges of the conduction band (CB) or the valence band (VB) to form band tail states [35]. It is evident that lattice strain engineering is one of the potential strategies to improve the electronic structure and carrier behavior of TiO_2. However, the extent of lattice distortion formation is limited by chemical equilibrium under the existing chemical strategies, which makes it difficult to have a considerable impact on the energy band structure [36]. Plasma immersion ion implantation (PIII) as a means of physical modification that is not restricted by the solid solubility of elements in the materials [37]. In addition, it is possible to introduce almost all elements into the target materials without introducing any impurity elements. After PIII, the thermal treatment processes usually activate the dopant and exacerbate the degree of lattice distortion [38]. Cu, as an essential trace element in the human body, promotes cell proliferation, angiogenesis and collagen deposition [39]. Moreover, the different ion radius and valence states between Cu and Ti is beneficial to the formation of lattice distortions of Cu doped TiO_2 in the process of thermal reduction [40,41].

Hence, we constructed a Cu-doped defective TiO_2 metastructure coating (Cu-TiO_x) on Ti surface by micro-arc oxidation (MAO), PIII and
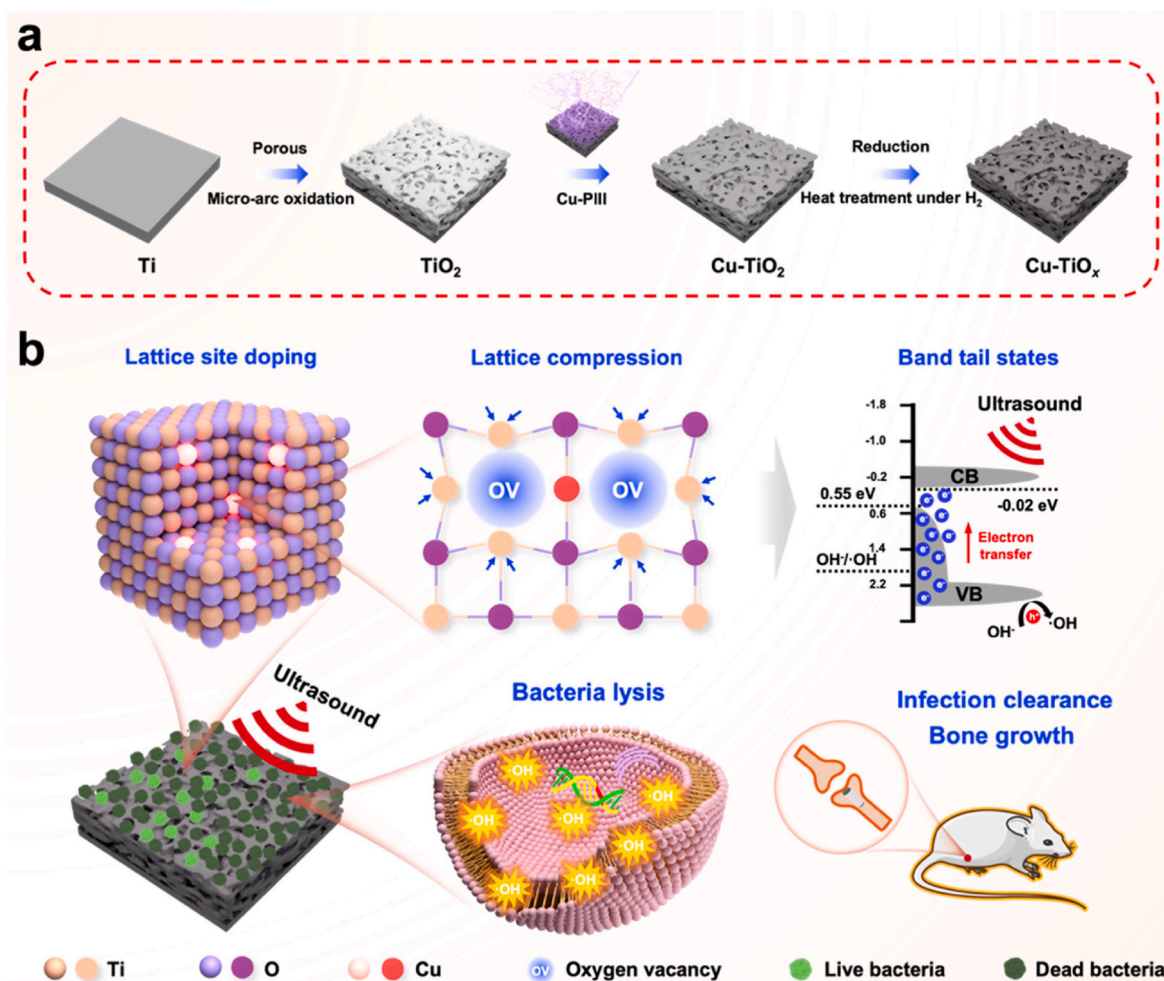
Scheme 1. Schematic illustration of (a) synthesis processes for TiO_2, Cu-TiO_2 and Cu-TiO_x. (b) Cu-TiO_x metastructure coating sonodynamic mechanism and sonodynamic antibacterial therapy.

thermal reduction treatment (Scheme 1). Cu atoms were redistributed during thermal reduction treatment, resulting in lattice distortions. Remarkably, the lattice distortions produced band tail states, which facilitated the separation of electron-hole pairs. Cu-TiO$_x$ metastructure coating can effectively eradicate bacterial infections by SDT and possessed osteogenic properties. This work may make a valuable contribution to the design of efficient SDT coatings based on lattice distortion and metastructure engineering.

2. Results and discussion

2.1. Characterization of Cu-TiO$_x$ metastructure coating

The SEM images of Ti, TiO$_2$, Cu-TiO$_2$, TiO$_x$ and Cu-TiO$_x$ are shown in Fig. 1a. The surface of pickled Ti was relatively rough, with ridged protrusions. TiO$_2$ exhibited a porous structure typical of MAO coatings, with highly interconnected pores and an average pore size of about 3 μm. Unlike the isolated pores observed in conventional MAO coatings, $[B_4O_7]^{2-}$ migrated into the plasma channel during MAO to participate in the discharge, and then was converted to B_2O_3 above 900 °C. The B_2O_3 in the molten state dissolved in the TiO$_2$ deposited around the discharge channel [42–44]. Therefore, continuous cascade discharges occurred, leading to interconnected pores. Under high-magnification SEM, it can be observed that the surface of titanium dioxide is relatively smooth and flat, with nanoscale pores present. The Cu-TiO$_2$ sample also exhibited a connected porous structure, and the surface was smooth, which indicated that Cu ion implantation did not significantly damage the morphology of TiO$_2$. On the contrary, due to the etching effect of hydrogen plasma under high temperature, the TiO$_x$ surface was uneven and the roughness was significantly increased. It is worth noting that the surface morphology of the Cu-TiO$_x$ sample was similar to that of TiO$_x$, and there were no Cu particles on the surface, which indicated that Cu atoms did not aggregate on the surface during the thermal reduction treatment.

The XRD pattern of TiO$_2$ showed characteristic diffraction peaks of Ti and sharp rutile phase TiO$_2$, indicating a high degree of crystallinity (Fig. 1b). The sharp rutile phase characteristic diffraction peaks were also observed in the Cu-TiO$_2$ sample. In addition, there were no characteristic diffraction peaks of Cu or copper oxide in it, which may be due to the high dispersion of Cu atoms in the coating. The diffraction peaks of TiO$_x$ were significantly weakened and broadened after the reduced calcination treatment, indicating that its crystal structure was significantly damaged. It is worth noting that the diffraction peak intensity of Cu-TiO$_x$ was weaker than that of TiO$_x$. More importantly, the diffraction peaks of the (110) and (101) crystal planes of Cu-TiO$_x$ were shifted to higher angles (Fig. 1c and d), which implied that the spacing of the crystal planes was decreased. The cell parameters of the different samples were obtained by Bragg's law. As shown in Table S1, the c-axis direction length and the cell volume of Cu-TiO$_x$ decreased, but there was no significant change in the cell volume for Cu-TiO$_2$ and TiO$_x$. Therefore, it is likely that Cu atoms were doped into the lattice of TiO$_2$ during the thermal reduction treatment.

The elemental valence states were further analyzed by X-ray photoelectron spectroscopy (XPS), as shown in Fig. 1e, f and 1g. There were two peaks for TiO$_2$ and Cu-TiO$_2$ at 458.5 eV (Ti 2p$_{3/2}$) and 464.4 eV (Ti 2p$_{1/2}$), indicating that Ti only existed in the form of Ti^{4+}. In contrast, there are two additional Ti^{3+} signal peaks at 456.4 eV and 461.5 eV for TiO$_x$ and Cu-TiO$_x$ samples due to the thermal reduction treatment. And Cu element was also reduced to a lower state (Fig. 1g). The Ti^{3+} content of TiO$_x$ and Cu-TiO$_x$ was calculated to be 21.93 % and 33.38 % respectively (Ti^{3+} content: Cu-TiO$_x$ > TiO$_x$), which meant that there were more oxygen defects in Cu-TiO$_x$ sample. The O 1s XPS high-resolution spectrum clearly showed that lots of oxygen vacancies (with a binding energy of 531.4 eV [45]) were introduced during the reduced calcination treatment (Figs. 1f), 23.83 % for TiO$_x$ and 38.78 % for Cu-TiO$_x$. It can be seen that the content of Ti^{3+} and oxygen vacancies

in Cu-TiO$_x$ sample were both higher than those in TiO$_x$, which was attributed to the doping of Cu atoms. Based on these data, it can be inferred that Cu atoms doped into the TiO$_2$ lattice during thermal reduction treatment, which replaced the Ti lattice sites and broke the original lattice coordination. Specifically, substitutional doping of Cu atoms in an oxygen-deficient environment induced chemical compensation effect, which led to the escape of O atoms from the lattice sites to form oxygen vacancies. Oxygen vacancies not only induced the generation of Ti^{3+} [46], but also caused localized collapse of the lattice structure.

As mentioned above, Cu atoms redistributed during thermal reduction treatment, resulting in the formation of lattice distortions. To elucidate this unusual phenomenon, we observed and analyzed the microstructures of the Cu-TiO$_x$ sample by transmission electron microscopy (TEM). In order to avoid distortion of the sample during thinning, the focused ion beam (FIB) working area was selected on the hole wall with a relatively flat surface (Fig. S1) to ensure the authenticity of the sample microstructure. As shown in Fig. S2, the thickness of the sample after FIB thinning was about 54 nm, which met the requirement of TEM. Combining the research of our research group and other research groups [47–51], the distribution of Cu atoms in the TiO$_2$ coating is closely related to the depth from the surface. Therefore, regions 40 nm and 300 nm away from the coating surface were selected as Region I and Region II, respectively (Fig. 2a), to comparatively illustrate the lattice distortions caused by Cu atom doping.

The specific location of Region I is shown in the red box in Fig. 2b, where the lattice structure was affected by Cu atoms doping so that it was considered as "outer layer with Cu atoms doping". As shown in Fig. 2c and S3, a large number of dislocations and planar vacancies were observed in Region I. The fast Fourier transformation (FFT) showed the special elongated diffraction spots of the planar vacancies (Fig. 2c inset). Fig. 2d shows the strain mapping of Region I along the xx direction, revealing large strain fluctuations caused by high-density dislocations and planar vacancies, in which compressive strain dominated. In order to further analyze the impact of Cu atoms doping, the lattice structures of regions C-1, C-2 and C-3 were selected. As shown in Fig. 2e, region C-1 corresponded to the (101) crystal plane of the rutile phase TiO$_2$ (normal crystal plane spacing of about 0.25 nm [52,53]), which exhibited lattice distortions, with a crystal plane spacing of 0.228 nm. The lattice was under compressive strain in the xx, yy, xy, and yx directions (Fig. 2f), which was consistent with the XRD analysis results (Fig. 1d). In particular, 3D atomic imaging (Fig. S4a) and the corresponding lattice line scan (Fig. S4b) in structural domain C-1 revealed obvious atomic defects in Cu-TiO$_x$, implying that Cu atoms doping into the lattice introduced oxygen vacancies, which was consistent with the XPS analysis (Fig. 1g). Similarly, lattice distortions were also present in the C-2 and C-3 regions (Figs. S5a and 5b), with a (101) crystal plan spacing of 0.229 nm.

Region II was 300 nm away from the sample surface (Fig. 2g) and was too deep for Cu ion implantation, so it was defined as the "inner surface layer without Cu atoms doping". Unlike Region I, the lattice structure of Region II was relatively complete, with low dislocation density and strain fluctuations (Fig. 2g–i), and the corresponding FFT showed independent diffraction spots (Fig. 2h inset). Meanwhile, the rutile TiO$_2$ (101) crystal plane in Fig. 2j was not compressed or stretched, and the spacing between the crystal planes was 0.243 nm. As revealed by 3D atomic imaging and lattice line scanning analysis (Figs. S6a and S6b), the crystal planes in Region II were complete and almost free of atomic defects. As shown in Figs. S7a and S7b, the undamaged lattice structures were also observed in the H-2 and H-3 regions. Comparative analysis of the TEM images of Region I and Region II reveals that Cu atom doping indeed caused lattice distortions in TiO$_2$ lattice. Lattice distortions affect the energy band structure of Cu-TiO$_x$ metastructure coating, which will be discussed later.
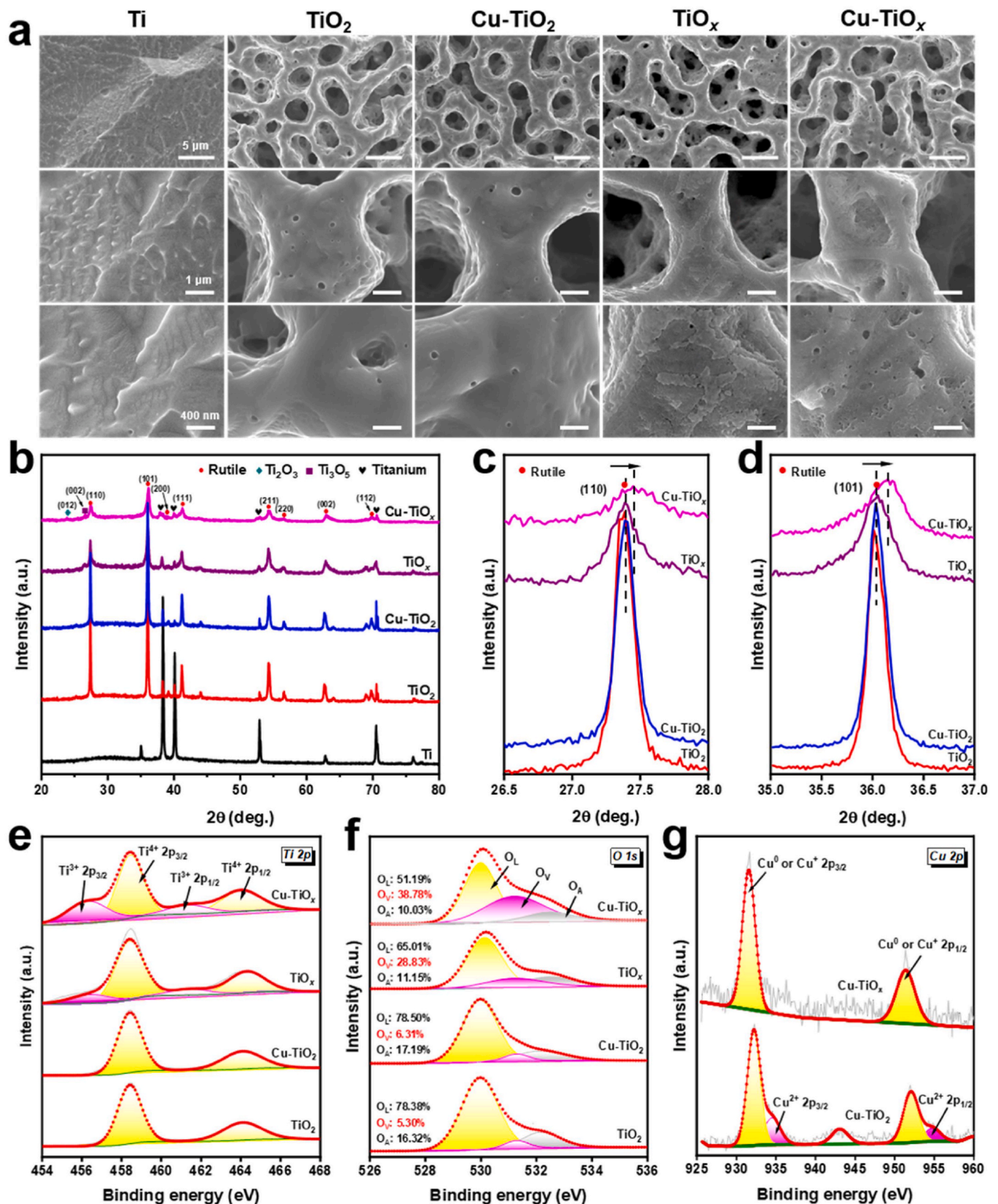
Fig. 1. Properties of Cu-TiO$_x$ metastructure coating. (a) SEM images of Ti, TiO$_2$, Cu-TiO$_2$, TiO$_x$ and Cu-TiO$_x$. (b) XRD patterns of Ti, TiO$_2$, Cu-TiO$_2$, TiO$_x$ and Cu-TiO$_x$. (c) Enlarged patterns in the ranges of 26.5–28° and (d) 35–37° of XRD patterns. High-resolution XPS spectra of (e) Ti and (f) O elements for TiO$_2$, Cu-TiO$_2$, TiO$_x$ and Cu-TiO$_x$ samples. (g) High-resolution XPS spectra of Cu element for Cu-TiO$_2$ and Cu-TiO$_x$ samples.

Fig. 2. Microstructural characterization of Cu-TiO$_x$ metastructure coating. (a) FIB image of Cu-TiO$_x$. (b) TEM bright-field image of Region A marked in (a). (c) HRTEM image of Region I and inset shows the fast Fourier transformation (FFT) image for (c). (d) Geometric phase analysis (GPA) in the xx direction of (c). (e) The Inverse Fast Fourier Transformation (IFFT) image of the area C-1 in (c). (f) GPA in the xx, xy, yx, and yy directions of (e). (g) TEM bright-field image of Region B marked in (a). (h) HRTEM image of Region II and inset is the FFT image for (h). (i) GPA in the xx direction of (h). (j) The IFFT image of the area H-1 in (h).

2.2. Ultrasonic performance and band structure

The outstanding sound-absorbing properties and acoustic-to-thermal conversion capacity of porous materials often attract the attention of researchers [54]. Hyperthermia is an effective measure to kill bacteria [55]. Consequently, we evaluated the acoustic-to-thermal conversion property of Cu-TiO$_x$ metastructure coating. During ultrasonic irradiation, the temperature of TiO$_2$, TiO$_x$, Cu-TiO$_2$ and Cu-TiO$_x$ gradually increased, and Cu-TiO$_x$ reached 53.1 °C at 10 min (Fig. 3a). Nevertheless, the temperature of the Ti surface can only reach a maximum of 42 °C, which was not sufficient to significantly kill bacteria. The results of the acoustic-to-thermal conversion curves were further supported by the real-time infrared images shown in Fig. 3b. The acoustic-to-thermal conversion capabilities of TiO$_2$, TiO$_x$, Cu-TiO$_2$, and Cu-TiO$_x$ were almost the same, which indicated that Cu ion implantation and reduction heat treatment did not affect the acoustic-to-thermal property of Cu-TiO$_x$ metastructure coating. Compared with Ti, TiO$_2$, TiO$_x$ and Cu-TiO$_2$, the ultrasonic current density of Cu-TiO$_x$ was significantly improved (Fig. 3c), indicating that it had an excellent US-triggered electron transition effect. Cu-TiO$_x$ metastructure coating can respond to US to achieve high electron-hole pairs separation efficiency, which was conducive to the improvement of sonocatalytic performance. Methylene blue (MB) can be oxidatively degraded by highly reactive ROS. Therefore, the sonocatalytic performance of Cu-TiO$_x$ metastructure coating

was evaluated by degrading MB through ultrasonic irradiation. As shown in Fig. 3d, the absorbance of MB in the Cu-TiO$_x$ group decreased significantly compared with that in the Ti, TiO$_2$ and Cu-TiO$_2$ groups, while the absorbance of MB in TiO$_x$ group decreased slightly. This result indicated that the lattice distortions significantly improved the sono-catalytic efficiency Cu-TiO$_x$ metastructure coating, which may be attributed to the lattice distortions changing the energy band structure of Cu-TiO$_x$ metastructure coating. Subsequently, the ESR test results showed that C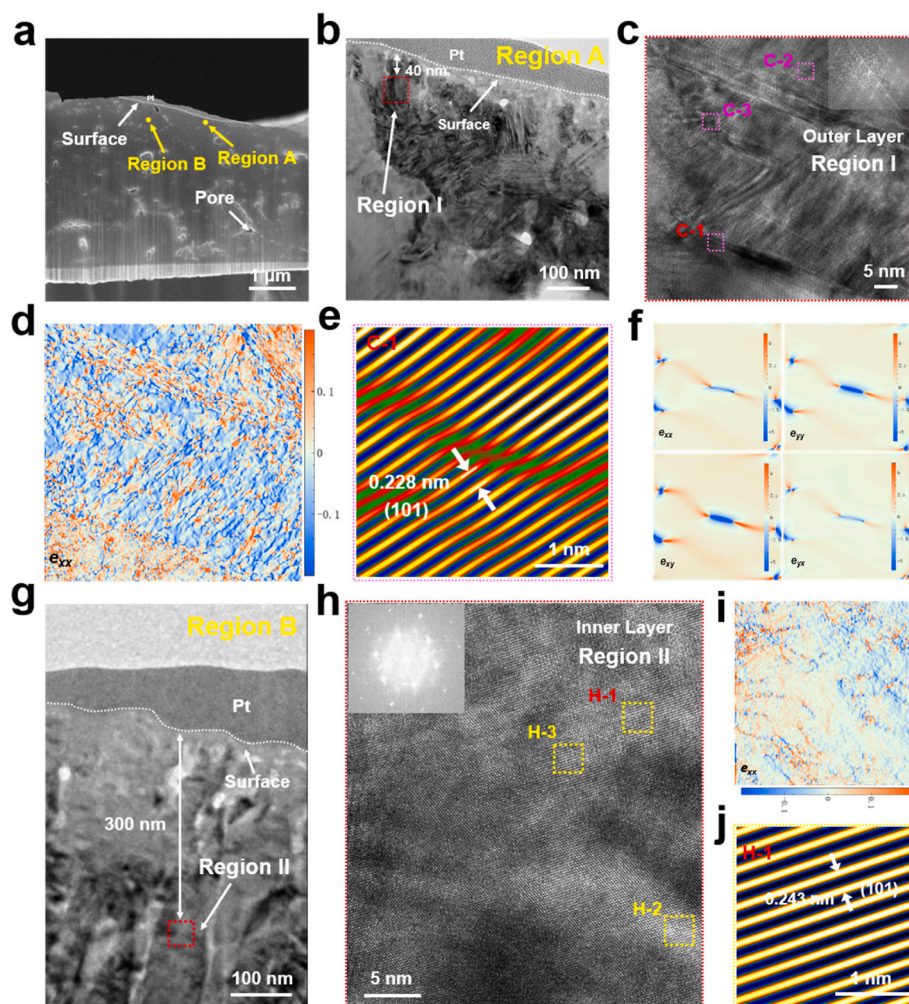u-TiO$_x$ metastructure coating can produce a strong ·OH characteristic peak during ultrasonic irradiation, while the ·O$_2^-$ and ^{1}O$_2$ signals remained silent (Fig. 3e–S8a and S8b).

In order to reveal the sonocatalytic mechanism and band structures, the electronic structures of TiO$_2$, TiO$_x$ and Cu-TiO$_x$ samples were further studied. Photoluminescence (PL) occurs with electron-hole pairs recombination in semiconductors, and the peak intensity is positively correlated with the electron-hole pairs recombination rate. As shown in Fig. 3f, the Cu-TiO$_x$ metastructure coating had the slowest electron-hole pair complexation rate, which was favorable for increasing the yields of ROS [56]. After thermal reduction treatment, TiO$_x$ and Cu-TiO$_x$ showed strong absorption tails in the whole visible light range (Fig. 3g). What's more, the absorbance of Cu-TiO$_x$ was significantly higher than that of TiO$_x$ and TiO$_2$. The band gaps of TiO$_x$ and Cu-TiO$_x$ were 2.21 eV and 2.03 eV, respectively, which were much smaller than the band gap of the original TiO$_2$ (2.92 eV, Fig. 3h). It is worth noting that the VB of TiO$_x$
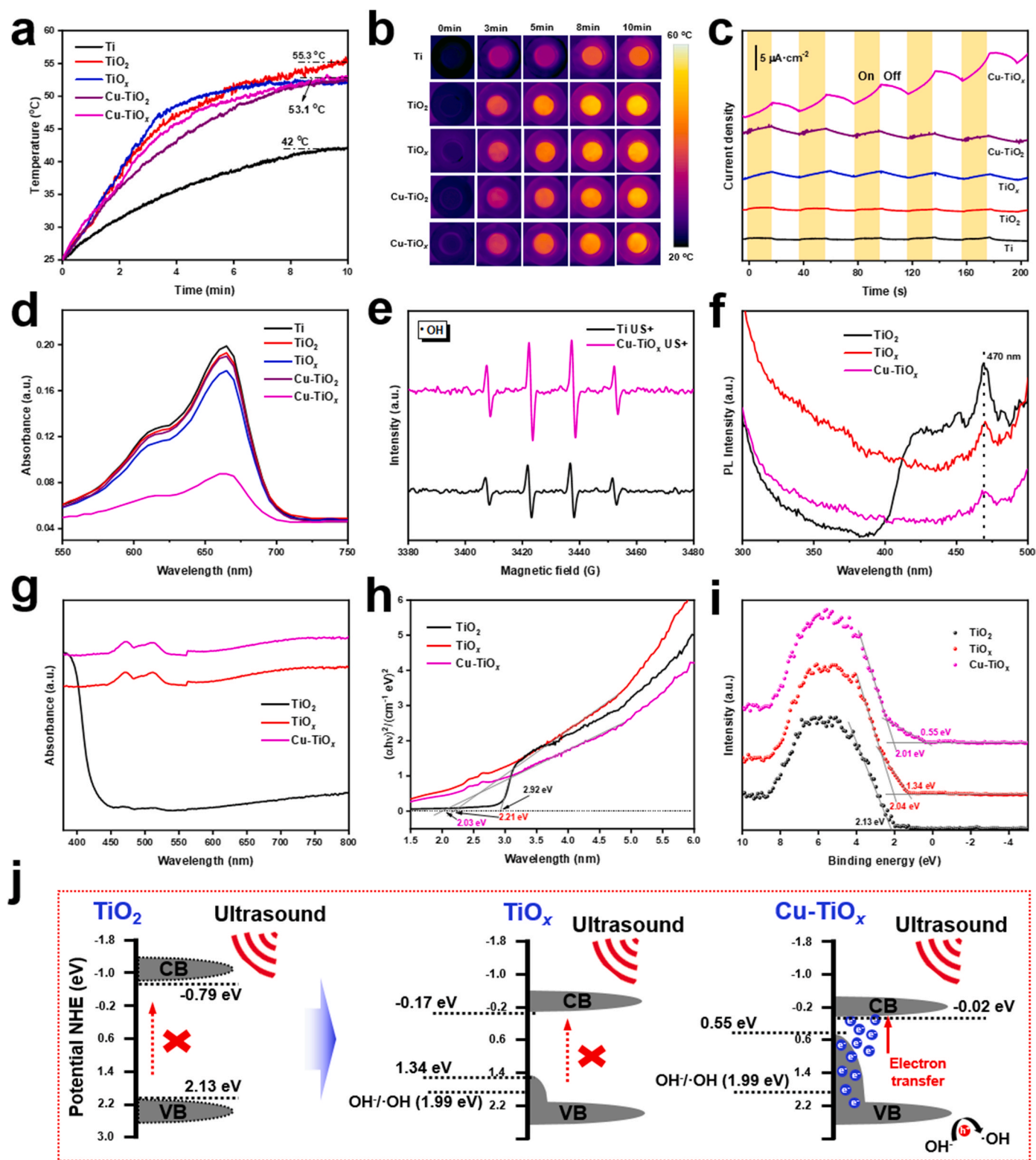
Fig. 3. Sonothermal property test, ultrasonic-triggered ROS and band gap structure. (a) Sonothermal property test and (b) real-time infrared image of different samples. (c) Ultrasonic current tests of Ti, TiO_2, TiO_x, $Cu-TiO_2$ and $Cu-TiO_x$ samples. (d) MB degradation test spectra of Ti, TiO_2, TiO_x, $Cu-TiO_2$ and $Cu-TiO_x$ samples under ultrasonic irradiation. (e) ESR image of ·OH. (f) PL emission spectra of TiO_2, TiO_x and $Cu-TiO_x$. (g) UV–vis absorption spectra, (h) band gaps, (i) VB-XPS and (j) band structure diagrams of TiO_2, TiO_x and $Cu-TiO_x$ samples.

and $Cu-TiO_x$ shifted upward (2.04 eV and 2.01 eV, respectively), and new band tail states were formed (Fig. 3i) [57].

The mechanisms for the ultrasonic dynamics and band structures were proposed using XPS valence band spectroscopy, ultraviolet–visible

(UV–vis) absorption spectroscopy and theoretical calculation (Fig. S9), as seen in Fig. 3j. Cu atoms diffused into the TiO_2 lattice and replaced Ti lattice sites during the thermal reduction treatment, resulting in the generation of a large number of Ti^{3+} and oxygen vacancies. On one

hand, this replacement behavior disrupted the original lattice structure and resulted in lattice distortions, which introduced multiple impurity energy levels in the band gap. They were continuously attached to VB to form band tail states. An additional potential advantage of these engineered distortions is that they provide trapping sites for carriers and prevent them from rapid recombination, thus promoting electron transfer and sonocatalytic reactions [58]. As shown in Figs. S9d–S9i, lattice distortion significantly enhanced the energy band structure of Cu-TiO$_x$ metastructure coating, which plays a key role in enhancing sonocatalytic performance. On the other hand, the presence of oxygen

vacancies in Cu-TiO$_x$ metastructure coating reduced the CB position (−0.02 eV) [59]. What's more, electron-hole pairs recombination was not easy to occur in Cu-TiO$_x$ metastructure coating (Fig. 3f). As a result, the electron-hole pairs in the Cu-TiO$_x$ metastructure coating separate rapidly under ultrasonic irradiation. The electrons easily jumped to the CB with the help of band-tailed states and a large number of holes remain in VB. Finally, the holes combine with OH- thus producing a large amount of ·OH.
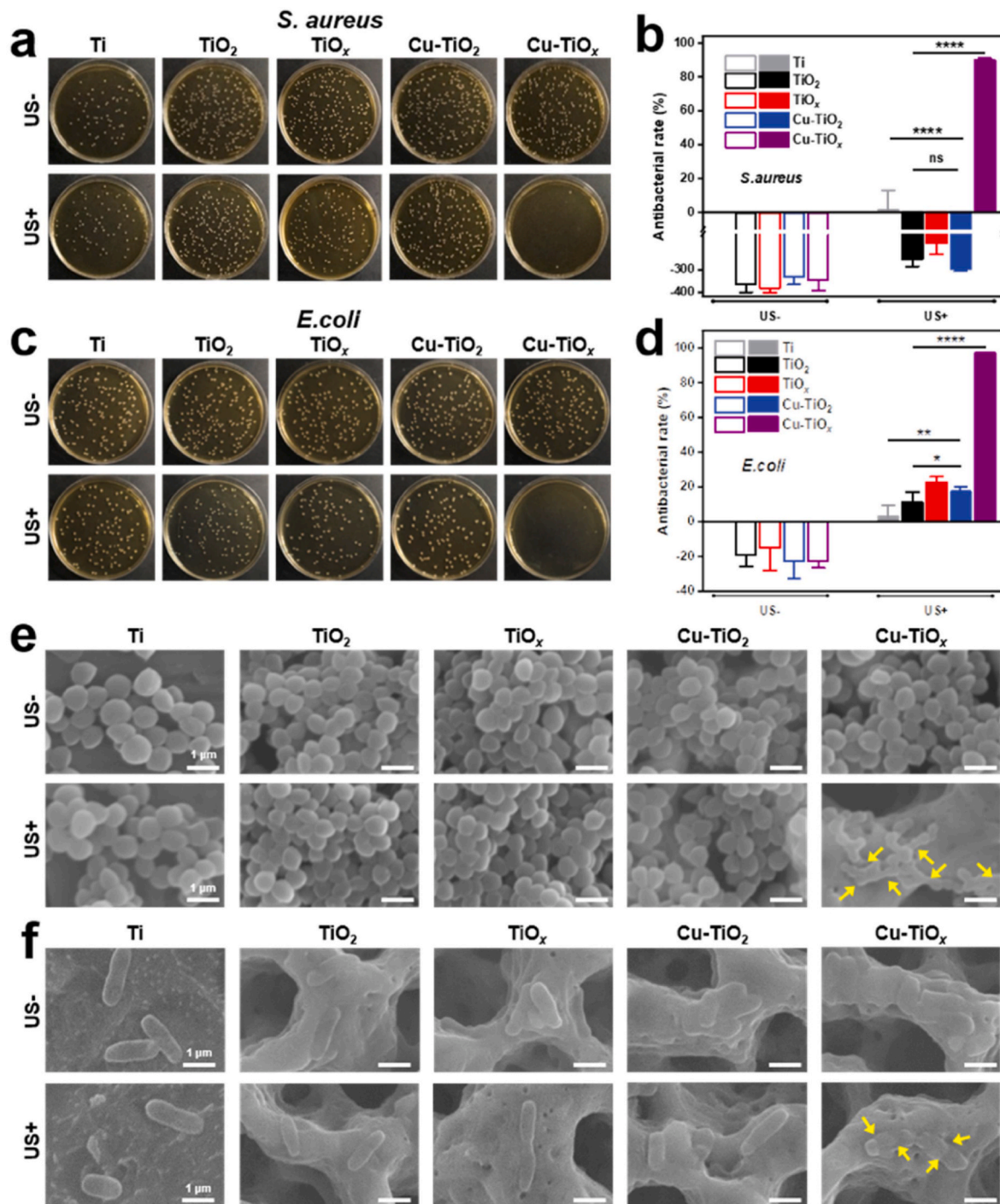
Fig. 4. Antibacterial performance study of Cu-TiO$_x$ metastructure coating *in vitro*. (a) Colony growth chart of *Staphylococcus aureus* with and without US treatment and (b) the antibacterial rate. (c) Colony growth chart of *Escherichia coli* with and without US treatment and (d) the antibacterial rate. (e, f) SEM images of *Staphylococcus aureus* and *Escherichia coli* on different sample surfaces with and without US treatment.

2.3. Antibacterial activity of Cu-TiO$_x$ metastructure coating in vitro

Bacterial infections tend to be random and highly recurrent during the service life of implants. Therefore, immediate response treatment after implant infection is crucial. Fig. 4a–d evaluate the antibacterial rate of Cu-TiO$_x$ metastructure coating against *Staphylococcus aureus* (*S. aureus*) and Escherichia coli (*E. coli*) using the plate coating method. As shown in Fig. 4a–c, Ti did not exhibit an antibacterial effect after 10 min of US irradiation, TiO$_2$, TiO$_x$ and Cu-TiO$_2$ exhibited a slight killing effect on bacteria due to the excellent acoustic-to-thermal conversion. Excitingly, Cu-TiO$_x$ showed a significant bactericidal effect after 10 min of ultrasonic irradiation. The antibacterial rates of Cu-TiO$_x$ against *S. aureus* and *E. coli* reached 90.00 % and 97.24 %, respectively (Fig. 4b–d). As seen in Fig. S10a, no significant antibacterial rings existed around all samples and the release of copper ions from Cu-TiO$_2$ and Cu-TiO$_x$ under ultrasonic irradiation was minimal, which did not cause a killing effect on bacteria (Fig. S10b). What's more, copper ion release curves for 21 days showed that Cu-TiO$_2$ and Cu-TiO$_x$ released too little copper ions to have a killing effect on the bacteria (Fig. S11). The above results confirmed the excellent antibacterial SDT of Cu-TiO$_x$ metastructure coating *in vitro*. The morphological characteristics of *S. aureus* and *E. coli* can further reflect the growth of bacteria on the sample surfaces. As shown in Fig. 4e–f, when samples were not irradiated by US, the forms of *S. aureus* (spherical) and *E. coli* (rod-shaped) were normal, they were full and round. Although the *S. aureus* and *E. coli*

on the Ti, TiO$_2$, TiO$_x$ and Cu-TiO$_2$ surfaces were not significantly affected, the *S. aureus* and *E. coli* growing on the Cu-TiO$_x$ surface were deformed to varying degrees (yellow arrows) after 10 min of ultrasonic irradiation, with the bacterial membrane clearly wrinkled and shrunk into a ball. The above results show that Cu-TiO$_x$ metastructure coating can achieve a significant killing effect on bacteria based on its excellent SDT and the antibacterial properties are broad-spectrum.

2.4. Osteogenic property of Cu-TiO$_x$ metastructure coating in vitro

Photographs of rBMSCs cytoskeleton staining on different sample surfaces at 1, 4 and 24 h are shown in Fig. 5a. Red represents the cytoskeleton and blue represents the nucleus. The rBMSCs on the TiO$_2$ surface expanded over a greater area during an hour of culture. Following a 4-h culture period, rBMSCs distributed evenly and took on polygonal overall forms on the surfaces of Ti, TiO$_2$, Cu-TiO$_2$, and Cu-TiO$_x$. After 24 h of culture, there was no discernible variation in the quantity of cells present on the surfaces of the samples belonging to each group. The cells were polygonal in shape and had numerous filopodia and lamellipodia. Compared with Ti, the adhesion of cells on TiO$_2$, TiO$_x$, Cu-TiO$_2$ and Cu-TiO$_x$ surfaces was better, with longer filopodia and more obvious lamellipodia. The proliferation activity of rBMSCs cultured on Ti, TiO$_2$, TiO$_x$, Cu-TiO$_2$ and Cu-TiO$_x$ surfaces for 1, 4 and 7 days is shown in Fig. 5b. After 1 day of culture, there was no significant difference in the proliferation activity of cells on the surfaces of the
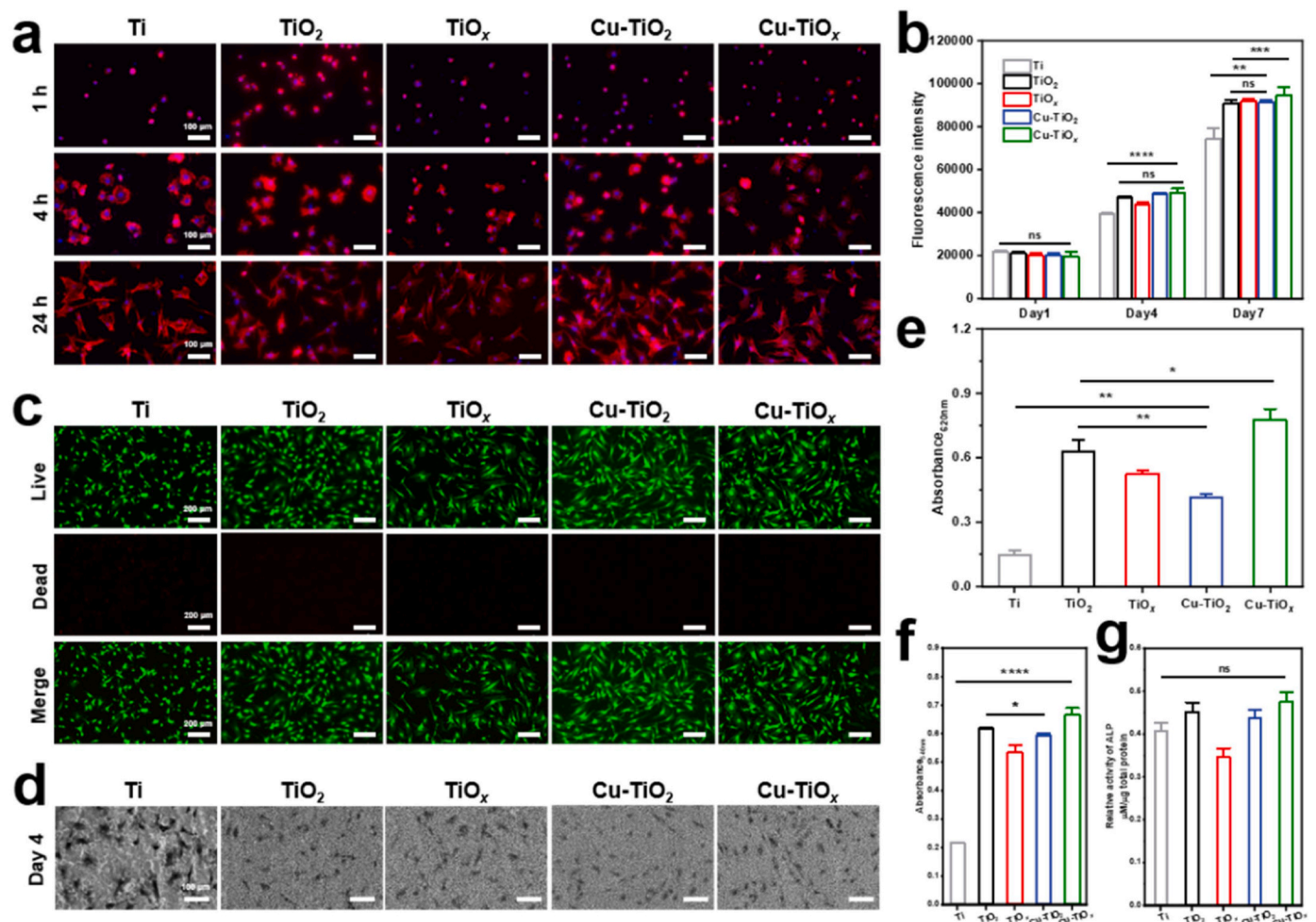
Fig. 5. rBMSCs growth on different sample surfaces to evaluate osteogenic activity *in vitro*. (a) Fluorescence staining of the cytoskeleton of cells cultured on different sample surfaces at 1, 4 and 24 h. (b) Quantitative results of proliferation activity of cells cultured on different sample surfaces at 1, 4 and 7 days. (c) Fluorescence images of live/dead staining (green/red) of cells cultured on different sample surfaces at 4 days. (d) SEM images of cells cultured on different sample surfaces at 4 days. Quantitative analysis of (e) collagen secretion,(f) extracellular matrix mineralization and (g) ALP activities of Ti, TiO$_2$, TiO$_x$, Cu-TiO$_2$ and Cu-TiO$_x$.

various samples. After 4 days of culture, the activity of rBMSCs on the TiO$_2$, TiO$_x$, Cu-TiO$_2$ and Cu-TiO$_x$ surfaces was slightly higher than that on Ti surface, and the cell activity on TiO$_x$ surface was lower than that of the other three groups. After 7 days of culture, the cell activity on TiO$_2$, TiO$_x$, Cu-TiO$_2$ and Cu-TiO$_x$ surfaces was significantly higher than that on Ti surface, and the cell activity on the Cu-TiO$_x$ surface was the highest. The higher the fluorescence intensity value, the stronger the cell viability, and the more obvious the cell proliferation. Fig. 5c displays fluorescent staining images of rBMSCs on the surfaces of different samples, and live and dead cells were stained green and red,

respectively. rBMSCs grew well on the surfaces of Ti, TiO$_2$, TiO$_x$, Cu-TiO$_2$ and Cu-TiO$_x$, and no dead cells were observed, indicating that Cu-TiO$_x$ exhibited superior cell safety. The cell morphologies on the surfaces of the different samples were observed using SEM, and the corresponding results are shown in Fig. 5d. The rBMSCs grew well on Ti, TiO$_2$, TiO$_x$, Cu-TiO$_2$ and Cu-TiO$_x$ surfaces, with normal morphologies and could spread well on the sample surfaces. Notably, the highest number of rBMSCs was found on the surface of Cu-TiO$_x$, which meant Cu-TiO$_x$ metastructure coating could promote cell proliferation most. What' more, Hemolysis test shows that TiO$_2$, TiO$_x$, Cu-TiO$_2$ and Cu-TiO$_x$ has

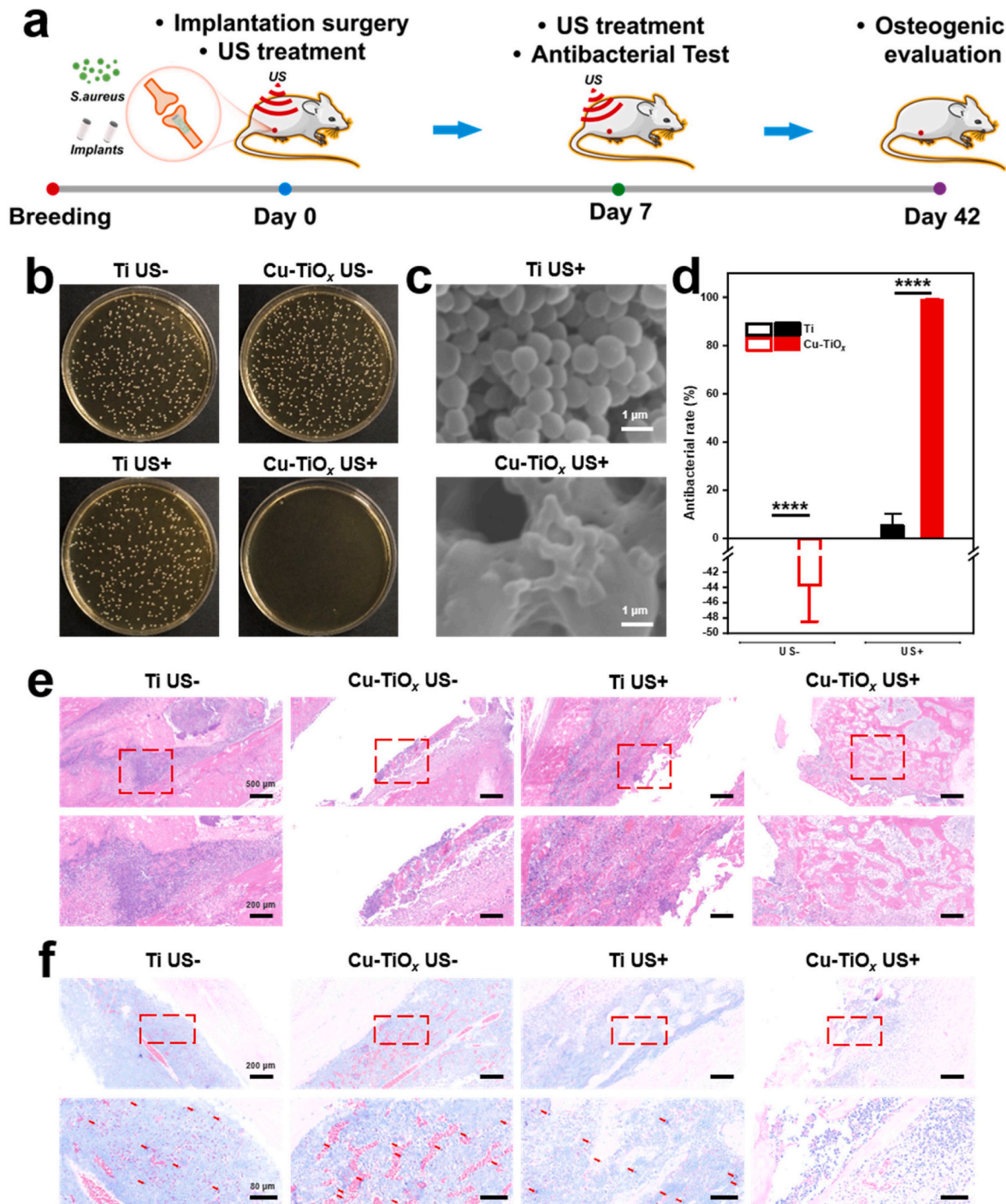**Fig. 6. Evaluation of the antibacterial performance of Cu-TiO$_x$ metastructure coating *in vivo*.** (a) Construction of the bacterial infection model in femoral implants. (b) Colony growth graphs of Ti and Cu-TiO$_x$ with and without US treatment, (c) corresponding bacterial SEM images and (d) antibacterial rate statistics. (e) H&E and (f) Gemisa staining images of infected bone tissue after 7 days.

good blood compatibility (Figs. S12 and S13).

Collagen secretion and extracellular matrix mineralization play important roles in osteogenesis [60]. The quantification of collagen secretion and extracellular matrix mineralization after 14 days of cell culture on sample surfaces are shown in Fig. 5e–f, respectively. The results showed that the collagen secretion and mineralization of the Cu-TiO$_x$ metastructure coating were significantly higher than Ti TiO$_2$, TiO$_x$, and Cu-TiO$_2$. Collagen and extracellular matrix mineralization staining results are consistent with quantitative results (Fig. S14). In addition, the ALP activity of Cu-TiO$_x$ were all higher than the other groups (Fig. 5g). The above results indicated that Cu-TiO$_x$ metastructure coating had excellent osteointegration function *in vitro*.

2.5. Antibacterial activity of Cu-TiO$_x$ metastructure coating in vivo

Considering the antibacterial capability and excellent biocompatibility of the Cu-TiO$_x$ metastructure coating *in vitro*, an infection model of rat femoral implants was constructed. In short, 5-week-old male Sprague Dawley rats were randomly divided into 4 groups, numbered Ti US -, Cu-TiO$_x$ US -, Ti US + and Cu-TiO$_x$ US +. The model construction and treatment strategy are shown in Fig. 6a. After the US treatment, the implants were removed and colony counting experiments were performed to evaluate the antibacterial rate *in vivo*. The results showed that the bacteria on Cu-TiO$_x$ metastructure coating were almost completely killed (Fig. 6b). It was observed by SEM that the bacteria on the surface of Ti US + survived normally, while the bacteria on the surface of Cu-TiO$_x$ US+ were shriveled (Fig. 6c). According to statistics, the antibacterial rate of Cu-TiO$_x$ US + group was as high as 98.97 % (Fig. 6d).

Inflammatory reactions usually occur in bacterial infections, so the inflammation of the tissues surrounding the implants was assessed by hematoxylin and eosin staining (H&E). As shown in Fig. 6e and S15, a large number of inflammatory cells can be observed in the tissues of rats in the Ti US - and Cu-TiO$_x$ US - groups. After 10 min of US treatment, tissue inflammation remained in the Ti US + group. In contrast, the tissue inflammation of rats in the Cu-TiO$_x$ US + group had subsided significantly and was almost negligible. In addition to the inflammatory response, bacteria on the implant surface can infiltrate into the surrounding tissue and cause further damage to the surrounding tissue. Giemsa staining (Fig. 6f) showed that there were a large number of bacterial colonies (red arrows) in Ti US -, Ti US + and Cu-TiO$_x$ US - groups, while there were almost no bacterial colonies in Cu-TiO$_x$ US + group. The H&E and Giemsa staining results showed that Cu-TiO$_x$ metastructure coating can be used to treat bone implant infections, and to remove residual bacteria in the tissue surrounding the implant. In summary, the SD rat femoral implant bacterial infection model fully demonstrates that Cu-TiO$_x$ metastructure coating can effectively remove bacterial infection, eliminate the inflammatory response and provide a harmonious environment for subsequent osseointegration when treated with US.

2.6. Osteogenic evaluation in a bacterial infection model

Bacterial infection of bone implants can seriously affect the growth of new bones around the implants, and peri-implant osseointegration is an important indicator of the length of time the implants serve. Therefore, after the bacterial infection of the implants is cleared, the growth of new bones around implants is crucial. In the above-mentioned bacterial infection model of rat femoral implants, the remaining rats were sampled 42 days after the implantation surgery for assessment of osteogenic performance after clearance of bacterial infection. Micro-CT was used to test the degree of regeneration of bone tissues around the implants. Micro-CT 2D and 3D imaging analysis (displayed in Fig. 7a–b) shows that after 42 days of implantation, the Ti US -, Ti US +, Cu-TiO$_x$ US - and Cu-TiO$_x$ US + groups all formed new bones, but the new bone mass was significantly higher in the Cu-TiO$_x$ US + group than in the other three groups. The quantitative results of the new bone volume are

shown in Fig. 7b, c and 7d. The new bone volume fraction (BV/TV) of Ti US -, Ti US +, Cu-TiO$_x$ US - and Cu-TiO$_x$ US + groups was 4.89 %, 4.49 %, 4.18 % and 7.89 %, respectively. In line with the BV/TV, the quantitative results of the new bone trabeculae (Fig. 7c–d) show that the number of new bone trabeculae and the density of the bone surface in the Cu-TiO$_x$ US + group were also significantly higher than those in the Ti US -, Ti US + and Cu-TiO$_x$ US - groups. The highest content of new bones in Cu-TiO$_x$ US + group was attributed to Cu-TiO$_x$ metastructure coating inherent bone promoting property and the favorable osteogenic environment after bacterial removal *in vivo*.

New bone tissues were stained light brown in osteocalcin immuno-histochemical staining (Fig. 7e), and the Cu-TiO$_x$ US + group had the greatest thickness of new bones around the implants. Safranin-O/fast green staining can distinguish cartilage from cortical bone (stained red and green, respectively). As can be seen in Fig. 7f, most of the new bones around the Cu-TiO$_x$ US + group were stained green, indicating that they existed in the form of cortical bone, while the new bones in the other three groups were mostly in the form of cartilage. The results of bacterial clearance and subsequent bone formation in the rat femur implant bacterial infection model mutually corroborate and together indicate that Cu-TiO$_x$ metastructure coating has the ability to achieve bacterial clearance in the early stage with SDT and promote bone integration in the later stage. To evaluate the biosafety of the Cu-TiO$_x$ metastructure coating, H&E staining was performed. It demonstrated the absence of any acute biotoxicity in the harvested major organs (heart, liver, spleen, lung, and kidney) across all groups (Fig. S16).

3. Conclusion

In summary, a US-triggered Cu-TiO$_x$ metastructure coating containing a host of lattice distortions was prepared *in situ* on the titanium surface for IAIs therapy. During the thermal reduction treatment, Cu atoms diffused into the lattice of TiO$_2$ and replaced the lattice sites of Ti. This process introduced lattice distortions, leading to the impurity energy levels connecting together and attaching to VB to produce band tail states. Under the stimulation of US, the electrons in VB can easily separate from the holes and cross the band gap with the help of band tail states, resulting in more ROS and a significant increase in SDT efficiency. Cu-TiO$_x$ metastructure coating showed more than 90 % inhibition against both *S. aureus* and *E. coli* under ultrasonic irradiation. What's more, Cu-TiO$_x$ metastructure coating effectively promoted osseointegration after elimination of the bacterial infection. Overall, this metastructure and lattice distortion engineered Cu-TiO$_x$ coating possesses good US-triggered antibacterial ability, which provides a promising strategy for the design of SDT coatings and the therapy of IAIs.

4. Materials and methods

4.1. Preparation of Cu-TiO$_x$

Commercial titanium plates (10 mm × 10 mm × 1 mm) were ultrasonically cleaned twice for 5 min each in a mixture of HF and HNO$_3$. The volume ratio of HF, HNO$_3$ and ultrapure water was 1: 5: 4 (HF, China National Pharmaceutical Group Chemical Reagent Co., Ltd.; HNO$_3$, 68 %, China National Pharmaceutical Group Chemical Reagent Co., Ltd.). The sample obtained was called Ti. Ti and a cylindrical graphite electrolytic cell were used as the anode and cathode of Microarc oxidation (MAO), respectively. 0.1 M sodium tetraborate (Na$_2$B$_4$O$_7$·10H$_2$O) and 0.25 M KOH mixed liquid as the electrolyte. MAO was carried out using a constant voltage method with an oxidation voltage of 400 V, a frequency of 600 Hz, a duty cycle of 10 %, and a time of 8 min. The corresponding sample was named TiO$_2$. We installed the cathode target. Cylindrical metallic copper rods are used as cathode targets for Cu-PIII. And TiO$_2$ samples were placed in the sample chamber. Next, we evacuated the sample chamber. When the vacuum in the sample chamber reached 6 × 10^{-3} Pa, argon gas was passed in. At the
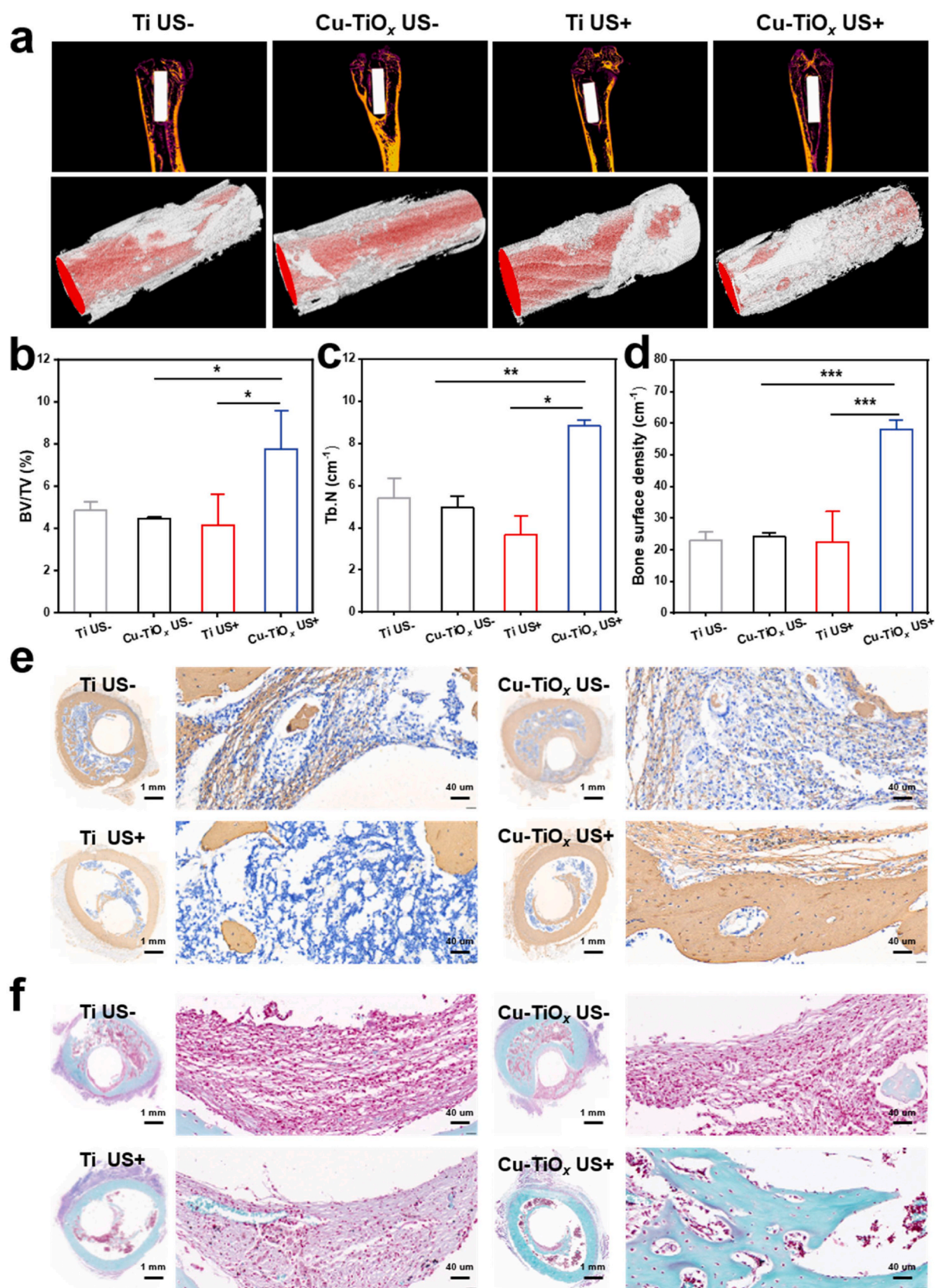
Fig. 7. Assessment of osteogenic property of Cu-TiO$_x$ metastructure coating *in vivo*. (a) 2D and 3D micro-CT images of Ti US -, Cu-TiO$_x$ US -, Ti US + and Cu-TiO$_x$ US +. (b) Quantitative statistical results of the ratio of new bone volume to total volume (BV/TV). (c) Number of trabeculae in new bone. (d) Surface density of new bone. (e) Immunohistochemical staining images of osteogenic proteins Col 1α in Ti US -, Ti US +, Cu-TiO$_x$ US - and Cu-TiO$_x$ US + (bone tissues were light-yellow). (f) Safranin-O/fast green staining images of groups Ti US -, Ti US +, Cu-TiO$_x$ US - and Cu-TiO$_x$ US + (cartilage was red and cortical bone was light-green).

same time, the cathode target was excited by a pulsed arc, which generated a copper plasma. Then the copper plasma entered the sample chamber through a magnetic filtration system to realize Cu-PIII of TiO$_2$. The specific implantation parameters are shown in Table 1. Subsequently, TiO$_2$ and Cu-TiO$_2$ were further treated with thermal reduction treatment to prepare TiO$_x$ and Cu-TiO$_x$. The atmosphere and temperature of thermal reduction treatment are shown in Table 2.

4.2. Material characterization

The morphology of samples was observed by scanning electron microscope (SEM, SU8220, Hitachi, Japan) to observe the sample morphology. X-ray photoelectron spectrometer (XPS, Thermo Scientific K-Alpha, Thermo Fisher, USA) was used to detect the surface elements and valence band positions. The phase composition of materials was detected by X-ray diffractometer (XRD, PHASER, Bruker, Germany). Thin sectioning of the coating was performed using a focused ion beam dual beam electron microscope (FIB, Helios G4 UX, FEI, USA), and then it was observed using a field emission transmission electron microscope (TEM, Tecnai G2 F20, FEI Electron Optics, Netherlands). Ultraviolet–visible spectroscopy was tested using a UV–vis spectrometer (Lambda 750, PerkinElmer, USA). The copper ion release was test by inductively coupled plasma (ICP, Prodigy Plus, Leeman Labs, USA).

4.3. Ultrasonic performance test

Sonocatalytic performance test: The sonocatalytic performance of Cu-TiO$_x$ was evaluated by testing the degradation of methylene blue (MB) solution (4 ppm). First, the samples were placed in a 24-well plate, 1 ml of MB solution was added, and then the samples were irradiated with US (1.5 W/cm^2, 50 % duty cycle, 1 MHz) for 10 min. The absorbance in the 500–750 nm band was measured by multimode microplate reader (Bio Tek Cytation 5, Agilent, USA).

Sonothermal performance test: We placed the sample to a 24-well cell culture plate and added 1 mL of ultrapure water to each well containing the sample. To avoid the influence of the ultrasonic probe itself heating on the test, a 1 cm thick gel was placed between the ultrasonic probe and the cell culture plate. An infrared imager was used to detect the temperature change of the sample during ultrasonic irradiation (1.5 W/cm^2, 50 % duty cycle, 1 MHz) for 10 min.

Sonocurrent test: The electroacoustic conversion properties of the samples were detected by an electrochemical workstation (AUTO LAB PGSTAT128N, Metrohm, Switzerland). Reference electrode, counter electrode and working electrode were saturated mercuric oxide electrode, platinum electrode and samples, respectively. 0.2 M Na$_2$SO$_4$ solution was used as the electrolyte, and US irradiation was used with 2.5 W/cm^2, 1 MHz, 100 % duty cycle.

Reactive Oxygen Species Stimulated by US: The types and signal strength of ROS were measured using an X-band benchtop continuous wave electron paramagnetic resonance spectrometer (EPR, EMXnano, Bruker, Germany), and the US irradiation time was 2 min for every sample, with 1.5 W/cm^{-2}, 50 % duty cycle and 1 MHz. 5,5-Dimethyl-1-pyrrolin-N-oxide (DMPO, 50 mM, in ultrapure water) was used as a trapping agent to identify hydroxyl radicals ($\bullet$OH) and superoxide anions ($\bullet$O$_2$), and 2, 2, 6, 6-tetramethylpiperidine (TEMP, 50 mM) was used to study singlet oxygen (^{1}O$_2$). The solvent for $\bullet$O$_2^-$ testing was

methanol, while ultrapure water was used as the solvent for the other two kinds of ROS.

4.4. Density functional theory calculations

We have employed the VASP to perform all the spin-polarized density functional theory (DFT) calculations within the generalized gradient approximation (GGA) using the Perdew-Burke-Ernzerhof (PBE) formulation. We have chosen the projected augmented wave (PAW) potentials to describe the ionic cores and take valence electrons into account using a plane wave basis set with a kinetic energy cutoff of 400eV. Partial occupancies of the Kohn−Sham orbitals were allowed using the Gaussian smearing method and a width of 0.05 eV. The electronic energy was considered self-consistent when the energy change was smaller than $10-6$ eV. A geometry optimization was considered convergent when the force change was smaller than -0.05 eV/Å2. Grimme's DFT-D3 methodology was used to describe the dispersion interactions among all the atoms. During structural optimizations of the surface models, the $5 \times 5 \times 1$ gamma-point centered k-point grid for Brillouin zone was used.

4.5. In vitro antibacterial test

Bacterial culture in vitro: Gram-negative Escherichia coli (*E. coli*, ATCC 25922) and Gram-positive Staphylococcus aureus (*S. aureus*, ATCC 25923) were selected for the bacterial test. To assess the antimicrobial efficacy of all samples, bacteria were used at a logarithmic phase concentration of 1×10^7 CFU/mL. Each sample was placed in a 24-well plate, and 500 μL of bacterial suspension was transferred to the 24-well plate containing the sample. The bacteria and samples were incubated together in a 37 °C constant temperature incubator for 6 h.

Bacterial plate count tests: The antibacterial ability of all samples was tested by the plate counting method. After 6 h of co-cultivation with the sample, the 24-well plate containing the sample and bacterial suspension was irradiated with US for 10 min. The ultrasonic power for *S. aureus* and *E. coli* was 0.8 W/cm^2, with a duty cycle of 50 % and a frequency of 1 MHz. The sample without ultrasonic irradiation was used as the control group. The concentration of the bacterial solution was diluted 10,000 times with 0.9 wt% sodium chloride solution. 100 μL of the bacterial suspension was evenly spread on an agar plate and incubated for a further 18 h at 37 °C. The corresponding antibacterial rate calculation formula is, Antibacterial rate (%) = (N$_{Ctrl}$ - N$_{Experiment}$)/N$_{Ctrl}$ $\times$ 100 % (N$_{Ctrl}$ represents the average colony count in Ti without US treatment, and N$_{Experiment}$ represents the average colony count in each group).

The copper ion release under ultrasonic excitation: Cu-TiO$_2$ and Cu-TiO$_x$ samples were immersed in 0.9 % NaCl solution for 6 h at a constant temperature of 37 °C. Then, US irradiation was used for 10 min with 0.8 W/cm^2, 1 MHz and 100 % duty cycle. ICP testing of immersion solutions to test for the release of copper ions.

Morphology of Bacteria: The bacteria and the samples were co-cultured for 6 h, with or without US irradiation of the samples with bacteria, as detailed in 2.4.1 and 2.4.2. The bacteria were fixed overnight using a 2.5 vol% glutaraldehyde solution (Sinopharm Chemical Reagent Co., Ltd.) at a volume of 1 ml/well. The samples were successively dehydrated in a gradient alcohol series (volume fraction: 30 %, 50 %, 75 %, 90 %, 95 % and 100 %) for 10 min each and allowed to air

Table 1
Experimental parameters of PIII.

	Target	Cathode
Pulse frequency/Hz	10	10
Pulse width/μs	500	500
Target voltage/kV	−15	–
Atmospheric pressure/Pa	6×10^{-3}	–
Implantation time/min	15	–

Table 2
Experimental parameters of thermal reduction treatment.

Time (min)	Temperature (°C)	Plasma power(W)	H$_2$ (sccm)	Ar (sccm)
70	700	0	10	80
10	700	0	10	80
60	700	50	10	80

dry. Finally, the morphology of bacteria was observed using scanning electron microscope (S3400N, HITACHI, Japan).

4.6. In vitro osteogenic evaluation

Cell culture: Rat bone marrow mesenchymal stem cells (rBMSCs) were used to evaluate the cytocompatibility of the samples. The cells were provided by the Cell Resource Center of the Chinese Academy of Sciences. The cell culture medium consisted of 89 % α-MEM basic culture medium, 10 % fetal bovine serum (FBS) and 1 % penicillin-streptomycin (Gibco, USA). The cells were cultured in an incubator filled with 5 % CO_2 at a temperature of 37 °C in a humidified atmosphere.

Cytocompatibility Evaluation: The samples were placed in a 24-well plate, the rBMSCs (2×10^4 cells/well) were seeded on the surface of the sample. AlamarBlue assay was used to evaluate cell viability for cells seeded within Ti, TiO_2, TiO_x, $Cu-TiO_2$ and $Cu-TiO_x$. The rBMSCs cultured for 7 days with cell culture medium refreshed every 3 days. After incubating for 1 day, the samples that attached with cells were transferred to a new 24-well plate, leaving behind the cells that escaped from samples. Cell culture medium supplemented with 10 % alamarBlue (Thermo Scientific) was added to wells with samples (test wells) and empty wells (negative control wells). After culturing for another 2 h in a 37 °C cell culture incubator, 100 μL of the culture solution was transferred from each well to a new 96-well plate to measure the absorbance at an excitation wavelength of 560 nm and an emission wavelength of 590 nm by a microplate reader (BioTek). The samples were then rinsed against PBS twice to remove residue alamarBlue, and 1 mL fresh cell culture medium was added to each well and refreshed every 3 days. The proliferative activity of rBMSCs was expressed by fluorescence intensity. Specially, the fluorescence intensity was calculated according to the proliferative activity of rBMSCs,

The proliferative activity of rBMSCs = A1 - A2

where A1 is the fluorescence intensity of the test wells; A2 is the fluorescence intensity of negative control wells (with media plus alamarBlue but no cells).

Cellular live/dead staining and morphological observation: The density of rBMSCs inoculated on the surface of the sample was 2×10^4 cells/well. After being cultured for 4 days according to the above method, the original medium was removed, the samples were washed twice with PBS, and 100 μL of a fluorescent staining solution (PBS solution containing 5 μM Ethidium homodier-1 and 2 μM calcein-AM) was added. Washing twice with PBS after incubating at 37 °C for 30 min, and the cell viability/death was observed by fluorescence microscope (OLYMPUS, DP72, Japan).

The cells were fixed overnight using a 2.5 vol% glutaraldehyde solution (Sinopharm Chemical Reagent Co., Ltd.) at a volume of 1 mL/well. The cells were successively dehydrated in a graded alcohol series (volume fraction: 30 %, 50 %, 75 %, 90 %, 95 % and 100 %) for 10 min each, air-dried naturally, and then the morphology of cells was observed using a scanning electron microscope (S3400N, HITACHI, Japan).

Cell adhesion and spreading: The rBMSCs were seeded at a density of 2×10^4 cells/well. After being placed in a 37 °C incubator for 1, 4 and 24 h, the original medium was removed, washed twice with PBS, and 1 ml of 4 % paraformaldehyde (PFA) solution was added to fix the cells. After permeabilizing the cells with 0.1 % (v/v) Triton X-100, the nuclei and cytoskeletons were stained with DAPI and FITC-phalloidin, respectively. Finally, the samples were photographed using a fluorescence microscope (OLYMPUS, DP72, Japan).

Alkaline phosphatase (ALP) activity: The sample surface was seeded with rBMSCs at a density of 5×10^3 cells/well and incubated in an incubator for 14 days. At the designated time point, the samples were placed in a new cell culture plate and washed twice with PBS. 0.5 mL of cell lysis solution was added to each well and lysed at 4 °C for 30 min. The collected cell lysate was centrifuged at 8000 rpm for 10 min in a

centrifuge. Taking 20 μL of the supernatant and adding it to p-nitro-phenyl phosphate (PNPP). Incubate at 37 °C for 30 min and stop the reaction with 1 M sodium hydroxide solution. After the solution was cooled to room temperature, the absorbance value (OD_{405}) at a wavelength of 405 nm was measured and the total ALP activity was calculated based on the standard curve. The total protein content in the supernatant can be detected using a BCA kit, and the relative activity of intracellular ALP on the sample surface can be normalized using the total protein content.

Collagen Secretion: The collagen secretion of stem cells on the sample surface was assessed using the Sirius Red (Sigma, USA) staining method. The sample surface was seeded with rBMSCs at a density of 5×10^3 cells/well and incubated in an incubator for 14 days. At the designated time point, the samples were rinsed twice with PBS and placed in a new 24-well plate. The cells were fixed with 4 % PFA for 30 min, rinsed twice with PBS, and then incubated with 0.1 % Sirius Red solution (dissolved in saturated picric acid). After 18 h, the stained samples were washed in 0.1 M acetic acid. For qualitative observation of collagen secretion, 0.1 M acetic acid was used to rinse the specimen repeatedly until no red color was precipitated, and the specimen was photographed by a stereomicroscope (fluorescence microscope bright field mode). To quantitatively detect the collagen content on the surface of the samples, 0.5 mL of elution solution (prepared by mixing methanol and 0.2 M NaOH solution in equal volumes) was added to each well, shaken well for 15 min, and the absorbance of the eluent at 540 nm (OD_{540}) was measured using a microplate reader.

Extracellular Matrix (ECM) Mineralization: The inoculation density of rBMSCs on the surface of every sample was 5×10^3 cells/well, and the samples were incubated in an incubator for 14 days. At the designated time point, the samples were placed in a new 24-well plate and the cells were washed twice with PBS for 3 min each. The cells on the surface of the samples were fixed with 75 % alcohol for 1 h. 500 μL of alizarin red (Sigma Aldrich, USA) solution was added to each well and transferred to a 4 °C refrigerator for 10 min. The stained samples were washed in ultrapure water. After staining, rinse the specimen repeatedly with ultrapure water until no color is precipitated (generally 3–5 times), and obtain the staining results using a stereomicroscope (fluorescence microscope bright field mode). Quantitative analysis of extracellular matrix mineralization: 0.5 mL of 10 % sodium hexadecyl pyridinium phosphate solution with a concentration of 10 mM was added to each well to elute the dye. The absorbance of the resulting solution at 620 nm was measured.

4.7. Blood compatibility evaluation

Hemolysis rate: The blood compatibility of the material surfaces was evaluated using whole blood from SD rats. The samples were placed in 24-well plates, and 1.5 mL of 0.9 % NaCl solution was added to each well, and equal amounts of 0.9 % NaCl solution and ultrapure water were added to the blank wells as the negative control and positive control groups, respectively, and kept warm at 37 °C for 30 min. 30 μL of human whole blood was added to the wells of the plates, and kept warm at 37 °C for 60 min after shaking. 1 mL of the extract was extracted from each well, and centrifuged at 3000 rpm for 5 min, and 100 μL was extracted from each well. Centrifuge 1 mL of leachate from each well at 3000 rpm for 5 min, and then add 100 μL of supernatant into a 96-well plate, and measure the absorbance at 545 nm with an enzyme counter. The hemolysis rate of the samples was calculated according to the following formula:

Hemolysis rate (%) = (OD_{sample} - $OD_{negative\ control}$) / ($OD_{positive\ control}$ - $OD_{negative\ control}$) × 100%

Platelet adhesion: The whole blood of healthy and fresh SD rats was centrifuged at 1500 rpm for 15 min, and the middle layer of yellowish platelet-rich plasma was added to the surface of the samples dropwise,

60 μL for each sample, and then placed in a 37 °C incubator to keep warm for 30 min. 0.9 % NaCl solution was rinsed twice, and 2.5 % glutaraldehyde (China National Pharmaceutical Corporation, Shanghai, China) was added to fix the platelets, and 500 μL was added for each sample, and then placed in a 4 °C refrigerator for 4 h. The platelets were fixed by adding 2.5 % glutaraldehyde (Shanghai, China) solution, 500 μL of each sample was added, and placed in the refrigerator at 4 °C for 4 h. The platelets were dehydrated using gradient concentrations of ethanol/water and ethanol/hexamethylsilanediamine solution, and the platelet adhesion pattern was observed by scanning electron microscope (S-3400N TypeI, Hitachi, Japan).

4.8. Animal experiments

Rat femur implant infection model: Ti and Cu-TiO$_x$ samples were implanted in the femurs of 5-week-old male Sprague-Dawley rats, and an implant infection model induced by *S. aureus* was constructed. The rats were anesthetized by intraperitoneal injection of 500 μL 4 % chloral hydrate, the hair at the femoral site was removed and the skin was disinfected. A sterile scalpel was used to cut through the skin and muscle tissue to expose the distal femur. A 2 mm hole was drilled between the rats' intercondylar eminences using a K-wire, parallel to the sagittal plane. Then, 20 μL of *S. aureus* bacterial solution (1×10^6 CFU/mL) was injected, followed by implantation of Ti and Cu-TiO$_x$. Finally, the muscle and skin tissues were sutured. The rats were treated with US for 10 min (1 W/cm^{-2}, 50 % duty cycle, 1 MHz) on day 0 and day 7 after implantation, respectively. Part of all rats were euthanized on the seventh day of implantation to evaluate the antibacterial ability of the implants by taking out the implants. For details of the bacterial smear plate operation, see 4.4. The remaining rats were kept for breeding, and after 42 days of implantation, they were euthanized. The femurs containing the implants were removed and immersed in 4 % PFA at 4 °C overnight for osteogenic evaluation.

Micro-CT test: Bone growth on the surface of the femoral implant was detected using a computed tomography scanner (Micro-CT, SkyScan 1276, Bruker, Germany) with the following scanning parameters: 70 kV, 200 mA, 9 mm resolution, 0.3° step size, and a 360° scan range. The implant position was assessed using 2D tomographic images, and the new bone growth on the implant surface was observed qualitatively using 3D reconstruction models. The volume of new bone was quantified using statistical analysis of the 3D models.

3D micro-CT images construction: We used NRecon software to reconstruct the scanned data. And the reconstructed data is the data needed for analysis. The implant and the surrounding new bones were precisely extracted from the bone by CTAn software. The data consisted of many images. To ensure the accuracy of the data, we first determined the range of images to analyze. Specifically, the top of the implant was used as the first image analyzed, and the bottom of the implant was used as the last image analyzed. We accurately selected the region of interest (ROI) with the draw tool. We saved the ROI additionally as a new file named VOI. We opened the VOI by CTAn software and separated the implant and the new bones around it by modulation threshold (The threshold range for new bones around the implant was 65–150 and the threshold range for implants was 150–255). Then, we saved the separated data separately and named them IMG 1 and IMG2 respectively. Finally, we loaded IMG 1 and IMG 2 into CTvox software to construct the 3D data of Micro-CT.

4.9. Statistical analysis

Statistical differences among groups were analyzed using GraphPad Prism 10 software, P. $P < 0.05$ indicates statistically significant differences between the two. $P < 0.05$ is indicated as *, $P < 0.01$ is indicated as **, $P < 0.001$ is indicated as ***, and $P < 0.0001$ is indicated as ****.

CRediT authorship contribution statement

Songsong Wang: Writing - review & editing, Writing - original draft, Methodology, Formal analysis, Data curation, Investigation, Whole experimentation. **Ji Tan:** Supervision, Methodology, Investigation, Formal analysis, Writing - review & editing, Conceptualization, Project design and administration. **Haifeng Zhang:** Writing - review & editing, Materials preparation experimentation. **Shiwei Guan:** Writing - review, Materials preparation experimentation. **Yibo Zeng:** Materials preparation experimentation, Animal experimentation. **Xiaoshuang Nie:** Methodology. **Hongqin Zhu:** Methodology. **Shi Qian:** Methodology. **Xuanyong Liu:** Writing - review & editing, Supervision, Funding acquisition, Resource.

Data availability

All data associated with this study are present in the paper or the supplemental information. Raw data are available upon request.

Ethics approval and consent to participate

The animal surgical procedures were conducted in accordance with the Guidelines for Care and Use of Laboratory Animals and approved by the Institutional Animal Care and Use Committee of Shanghai Rat&Mouse Biotech Co., Ltd (Protocol number: RM202405 (33)).

Declaration of interests

Xuanyong Liu is an editorial board member for Bioactive Materials and was not involved in the editorial review or the decision to publish this article. All authors declare that there are no competing interests.

Acknowledgments

Appendix A. Supplementary data

Supplementary data to this article can be found online at https://doi.org/10.1016/j.bioactmat.2025.02.028.

References

[1] W.P.J. Smith, B.R. Wucher, C.D. Nadell, K.R. Foster, Bacterial defences: mechanisms, evolution and antimicrobial resistance, Nat. Rev. Microbiol. 21 (8) (2023) 519–534, https://doi.org/10.1038/s41579-023-00877-3.

[2] E.K. Perry, L.A. Meirelles, D.K. Newman, From the soil to the clinic: the impact of microbial secondary metabolites on antibiotic tolerance and resistance, Nat. Rev. Microbiol. 20 (3) (2022) 129–142, https://doi.org/10.1038/s41579-021-00620-w.

[3] W. Tang, N.G. Fischer, X. Kong, T. Sang, Z. Ye, Hybrid coatings on dental and orthopedic titanium implants: current advances and challenges, BMEMat (2024) e12105, https://doi.org/10.1002/bmm2.12105.

[4] A. Khademi, A. Khandan, P. Iranmanesh, M. Heydari, Development of a 3D bioprinted alginate-gelatin hydrogel scaffold loaded with calcium phosphates for dental pulp tissue regeneration, Iran. J. Chem. Chem. Eng. (Int. Engl. Ed.) (2024), https://doi.org/10.1016/j.bprint.2020.e00105.

[5] P. Zhu, Y. Chen, J. Shi, Piezocatalytic tumor therapy by ultrasound-triggered and BaTiO$_3$-mediated piezoelectricity, Adv. Mater. 32 (29) (2020), https://doi.org/10.1002/adma.202001976.

[6] L. Wang, G. Li, L. Cao, Y. Dong, Y. Wang, S. Wang, Y. Li, X. Guo, Y. Zhang, F. Sun, X. Du, J. Su, Q. Li, X. Peng, K. Shao, W. Zhao, An ultrasound-driven immune-boosting molecular machine for systemic tumor suppression, Sci. Adv. 7 (43) (2021), https://doi.org/10.1126/sciadv.abj4796.

[7] X. He, Y. Lv, Y. Lin, H. Yu, Y. Zhang, Y. Tong, C. Zhang, Platinum nanoparticles regulated V$_2$C MXene nanoplatforms with NIR-II enhanced nanozyme effect for photothermal and chemodynamic anti-infective therapy, Adv. Mater. 36 (25) (2024), https://doi.org/10.1002/adma.202400366.

[8] X. Liu, M. Wang, L. Cao, J. Zhuang, D. Wang, M. Wu, B. Liu, Living artificial skin: photosensitizer and cell sandwiched bacterial cellulose for chronic wound healing, Adv. Mater. 36 (26) (2024), https://doi.org/10.1002/adma.202403355.

[9] T. Gu, Y. Wang, Y. Lu, L. Cheng, L. Feng, H. Zhang, X. Li, G. Han, Z. Liu, Platinum nanoparticles to enable electrodynamic therapy for effective cancer treatment, Adv. Mater. 31 (14) (2019), https://doi.org/10.1002/adma.201806803.

[10] Z. Lu, J. Gao, C. Fang, Y. Zhou, X. Li, G. Han, Porous Pt nanospheres incorporated with GOx to enable synergistic oxygen-inductive starvation/electrodynamic tumor therapy, Adv. Sci. 7 (17) (2020), https://doi.org/10.1002/advs.202001223.

[11] Y. Zhang, X. Wang, C. Chu, Z. Zhou, B. Chen, X. Pang, G. Lin, H. Lin, Y. Guo, E. Ren, P. Lv, Y. Shi, Q. Zheng, X. Yan, X. Chen, G. Liu, Genetically engineered magnetic nanocages for cancer magneto-catalytic theranostics, Nat. Commun. 11 (1) (2020), https://doi.org/10.1038/s41467-020-19061-9.

[12] J. Li, X. Liu, Y. Zheng, Z. Cui, H. Jiang, Z. Li, S. Zhu, S. Wu, Achieving fast charge separation by ferroelectric ultrasonic interfacial engineering for rapid sonotherapy of bacteria-infected osteomyelitis, Adv. Mater. 35 (13) (2023), https://doi.org/10.1002/adma.202210296.

[13] S. Duan, R. Wu, Y.-H. Xiong, H.-M. Ren, C. Lei, Y.-Q. Zhao, X.-Y. Zhang, F.-J. Xu, Multifunctional antimicrobial materials: from rational design to biomedical applications, Prog. Mater. Sci. 125 (2022), https://doi.org/10.1016/j.pmatsci.2021.100887.

[14] C. Chen, G. Chu, W. He, Y. Liu, K. Dai, J. Valdez, A. Moores, P. Huang, Z. Wang, J. Jin, M. Guan, W. Jiang, Y. Mai, D. Ma, Y. Wang, Y. Zhou, A janus Au-polymersome heterostructure with near-field enhancement effect for implant-associated infection phototherapy, Adv. Mater. 35 (3) (2023), https://doi.org/10.1002/adma.202207950.

[15] X. Song, Q. Zhang, M. Chang, L. Ding, H. Huang, W. Feng, T. Xu, Y. Chen, Nanomedicine-enabled sonomechanical, sonopiezoelectric, sonodynamic, and sonothermal therapy, Adv. Mater. 35 (31) (2023), https://doi.org/10.1002/adma.202212259.

[16] Y. Li, W. Chen, Y. Kang, X. Zhen, Z. Zhou, C. Liu, S. Chen, X. Huang, H.-J. Liu, S. Koo, N. Kong, X. Ji, T. Xie, W. Tao, Nanosensitizer-mediated augmentation of sonodynamic therapy efficacy and antitumor immunity, Nat. Commun. 14 (1) (2023), https://doi.org/10.1038/s41467-023-42509-7.

[17] B. Geng, J. Hu, Y. Li, S. Feng, D. Pan, L. Feng, L. Shen, Near-infrared phosphorescent carbon dots for sonodynamic precision tumor therapy, Nat. Commun. 13 (1) (2022), https://doi.org/10.1038/s41467-022-33474-8.

[18] S.A. Cummer, J. Christensen, A. Alu, Controlling sound with acoustic metamaterials, Nat. Rev. Mater. 1 (3) (2016), https://doi.org/10.1038/natrevmats.2016.1.

[19] J. Cha, K.W. Kim, C. Daraio, Experimental realization of on-chip topological nanoelectromechanical metamaterials, Nature 564 (7735) (2018) 229, https://10.1038/s41586-018-0764-0.

[20] L. Nie, D.A. Hutchins, L. Astolfi, T.P. Cooper, A.T. Clare, C. Adams, R.L. Watson, P. J. Thomas, D.M.J. Cowell, J.R. McLaughlan, S. Laureti, M. Ricci, S. Freear, A metallic additively manufactured metamaterial for enhanced monitoring of acoustic cavitation-based therapeutic ultrasound, Adv. Eng. Mater. 24 (4) (2022), https://doi.org/10.1002/adem.202100972.

[21] G. Ma, P. Sheng, Acoustic metamaterials: from local resonances to broad horizons, Sci. Adv. 2 (2) (2016), https://doi.org/10.1126/sciadv.1501595.

[22] B. Assouar, B. Liang, Y. Wu, Y. Li, J.-C. Cheng, Y. Jing, Acoustic metasurfaces, Nat. Rev. Mater. 3 (12) (2018) 460–472, https://doi.org/10.1038/s41578-018-0061-4.

[23] L. Huang, S. Huang, C. Shen, S. Yves, A.S. Pilipchuk, X. Ni, S. Kim, Y.K. Chiang, D. A. Powell, J. Zhu, Y. Cheng, Y. Li, A.F. Sadreev, A. Alu, A.E. Miroshnichenko, Acoustic resonances in non-Hermitian open systems, Nat. Rev. Phys. 6 (1) (2024) 11–27, https://doi.org/10.1038/s42254-023-00659-z.

[24] H. Tang, Y. Yang, Z. Liu, W. Li, Y. Zhang, Y. Huang, T. Kang, Y. Yu, N. Li, Y. Tian, X. Liu, Y. Cheng, Z. Yin, X. Jiang, X. Chen, J. Zang, Injectable ultrasonic sensor for wireless monitoring of intracranial signals, Nature 630 (8015) (2024), https://doi.org/10.1038/s41586-024-07334-y.

[25] G.-H. Lee, H. Moon, H. Kim, G.H. Lee, W. Kwon, S. Yoo, D. Myung, S.H. Yun, Z. Bao, S.K. Hahn, Multifunctional materials for implantable and wearable photonic healthcare devices, Nat. Rev. Mater. 5 (2) (2020) 149–165, https://doi.org/10.1038/s41578-019-0167-3.

[26] C.-C. Yu, A. Shah, N. Amiri, C. Marcus, M.O.G. Nayeem, A.K. Bhayadia, A. Karami, C. Dagdeviren, A conformable ultrasound patch for cavitation-enhanced transdermal cosmeceutical delivery, Adv. Mater. 35 (23) (2023), https://doi.org/10.1002/adma.202300066.

[27] S. Son, J.H. Kim, X. Wang, C. Zhang, S.A. Yoon, J. Shin, A. Sharma, M.H. Lee, L. Cheng, J. Wu, J.S. Kim, Multifunctional sonosensitizers in sonodynamic cancer therapy, Chem. Soc. Rev. 49 (11) (2020) 3244–3261, https://doi.org/10.1039/C9CS00648F.

[28] S. Liang, X. Xiao, L. Bai, B. Liu, M. Yuan, P.a. Ma, M. Pang, Z. Cheng, J. Lin, Conferring Ti-based MOFs with defects for enhanced sonodynamic cancer therapy, Adv. Mater. 33 (18) (2021), https://doi.org/10.1002/adma.202100333.

[29] Y. Zhao, J. Liu, M. He, Q. Dong, L. Zhang, Z. Xu, Y. Kang, P. Xue, Platinum-titania Schottky junction as nanosonosensitizer, glucose scavenger, and tumor microenvironment-modulator for promoted cancer treatment, ACS Nano 16 (8) (2022) 12118–12133, https://doi.org/10.1021/acsnano.2c02540.

[30] F. Gong, L. Cheng, N. Yang, Y. Gong, Y. Ni, S. Bai, X. Wang, M. Chen, Q. Chen, Z. Liu, Preparation of TiH$_{1.924}$ nanodots by liquid-phase exfoliation for enhanced sonodynamic cancer therapy, Nat. Commun. 11 (1) (2020), https://doi.org/10.1038/s41467-020-17485-x.

[31] W. Liu, R. Shao, L. Guo, J. Man, C. Zhang, L. Li, H. Wang, B. Wang, L. Guo, S. Ma, B. Zhang, H. Diao, Y. Qin, L. Yan, Precise design of TiO$_2$@CoO$_x$ heterostructure via

[32] S. Wen, W. Zhang, J. Yang, Z. Zhou, Q. Xiang, H. Dong, Ternary Bi$_2$WO$_6$/TiO$_2$-Pt heterojunction sonosensitizers for boosting sonodynamic therapy, ACS Nano 18 (34) (2024) 23672–23683, https://doi.org/10.1021/acsnano.4c08236.

[33] E. Pastor, M. Sachs, S. Selim, J.R. Durrant, A.A. Bakulin, A. Walsh, Electronic defects in metal oxide photocatalysts, Nat. Rev. Mater. 7 (7) (2022) 503–521.

[34] T.S. Bui, E.C. Lovell, R. Daiyan, R. Amal, Defective metal oxides: lessons from CO$_2$RR and applications in NO$_x$RR, Adv. Mater. 35 (28) (2023), https://doi.org/10.1038/s41578-022-00433-0.

[35] S. Sun, G. Shen, Z. Chen, L. Pan, X. Zhang, J.-J. Zou, Harvesting urbach tail energy of ultrathin amorphous nickel oxide for solar -driven overall water splitting up to 680 nm, Appl. Catal. B Environ. 285 (2021), https://doi.org/10.1016/j.apcatb.2020.119798.

[36] Y. Zhang, J. Liu, Y. Xu, C. Xie, S. Wang, X. Yao, Design and regulation of defective electrocatalysts, Chem. Soc. Rev. (2024), https://doi.org/10.1039/D4CS00217B.

[37] W. Li, X. Zhan, X. Song, S. Si, R. Chen, J. Liu, Z. Wang, J. He, X. Xiao, A review of recent applications of ion beam techniques on nanomaterial surface modification: design of nanostructures and energy harvesting, Small 15 (31) (2019), https://doi.org/10.1002/smll.201901820.

[38] Z. Hou, C. Cui, Y. Li, Y. Gao, D. Zhu, Y. Gu, G. Pan, Y. Zhu, T. Zhang, Lattice-strain engineering for heterogenous electrocatalytic oxygen evolution reaction, Adv. Mater. 35 (39) (2023), https://doi.org/10.1002/adma.202209876.

[39] W. Xie, Z. Guo, L. Zhao, Y. Wei, The copper age in cancer treatment: from copper metabolism to cuproptosis, Prog. Mater. Sci. 138 (2023), https://doi.org/10.1016/j.pmatsci.2023.101145.

[40] Z. Gong, W. Zhong, Z. He, Q. Liu, H. Chen, D. Zhou, N. Zhang, X. Kang, Y. Chen, Regulating surface oxygen species on copper (I) oxides via plasma treatment for effective reduction of nitrate to ammonia, Appl. Catal. B Environ. 305 (2022), https://doi.org/10.1016/j.apcatb.2021.121021.

[41] J. Feng, L. Wu, S. Liu, L. Xu, X. Song, L. Zhang, Q. Zhu, X. Kang, X. Sun, B. Han, Improving CO2-to-C2+Product electroreduction efficiency *via* atomic lanthanide dopant-induced tensile-strained CuOx catalysts, J. Am. Chem. Soc. 145 (17) (2023) 9857–9866, https://doi.org/10.1021/jacs.3c02428.

[42] V.V. Brazhkin, I. Farnan, K.-i. Funakoshi, M. Kanzaki, Y. Katayama, A.G. Lyapin, H. Saitoh, Structural transformations and anomalous viscosity in the B$_2$O$_3$ melt under high pressure, Phys. Rev. Lett. 105 (11) (2010), https://doi.org/10.1103/PhysRevLett.105.115701.

[43] M.S. Vasil'eva, V.S. Rudnev, L.M. Tyrina, I.V. Lukiyanchuk, N.B. Kondrikov, P. S. Gordienko, Phase composition of coatings formed on titanium in borate electrolyte by microarch oxidation, Russ. J. Appl. Chem. 75 (4) (2002) 569–572, https://doi.org/10.1023/A:1019508928852.

[44] A. dos Santos, J.R. Araujo, S.M. Landi, A. Kuznetsov, J.M. Granjeiro, L.A. de Sena, C.A. Achete, A study of the physical, chemical and biological properties of TiO$_2$ coatings produced by micro-arc oxidation in a Ca-P-based electrolyte, J. Mater. Sci. Mater. Med. 25 (7) (2014) 1769–1780, https://doi.org/10.1007/s10856-014-5207-3.

[45] Z.D. Dai, X.H. Li, Q. Chen, Y.T. Zhu, Z.P. Shi, X. Deng, C. Wang, H.R. Chen, Injectable responsive hydrogel delivery platform: enabling high tissue penetration and sonogenetic-like potentiating anti-tumor immunotherapy, Adv. Funct. Mater. 34 (19) (2024), https://doi.org/10.1002/adfm.202313723.

[46] Y. Sun, H. Ji, Y. Sun, G. Zhang, H. Zhou, S. Cao, S. Liu, L. Zhang, W. Li, X. Zhu, H. Pang, Synergistic effect of oxygen vacancy and high porosity of nano MIL-125 (Ti) for enhanced photocatalytic nitrogen fixation, Angew. Chem. Int. Ed. 63 (3) (2024), https://doi.org/10.1002/anie.202316973.

[47] F. Flatscher, J. Todt, M. Burghammer, H.S. Soreide, L. Porz, Y.J. Li, S. Wenner, V. Bobal, S. Ganschow, B. Sartory, R. Brunner, C. Hatzoglou, J. Keckes, D. Rettenwander, Deflecting dendrites by introducing compressive stress in Li$_7$La$_3$Zr$_2$O$_{12}$ using ion implantation, Small 20 (12) (2024), https://doi.org/10.1002/smll.202307348.

[48] H. Pazniak, M. Benchakar, T. Bilyk, A. Liedl, Y. Busby, C. Noël, P. Chartier, S. Hurand, M. Marteau, L. Houssiau, R. Larciprete, P. Lacovig, D. Lizzit, E. Tosi, S. Lizzit, J. Pacaud, S. Célérier, V. Mauchamp, M.L. David, Ion implantation as an approach for structural modifications and functionalization of Ti$_3$C$_2$T$_x$ MXenes, ACS Nano 15 (3) (2021) 4245–4255, https://doi.org/10.1021/acsnano.0c06735.

[49] C. Xia, X.H. Ma, X.M. Zhang, K.Q. Li, J. Tan, Y.Q. Qiao, X.Y. Liu, Enhanced physicochemical and biological properties of C/Cu dual ions implanted medical titanium, Bioact. Mater. 5 (2) (2020) 377–386, https://doi.org/10.1016/j.bioactmat.2020.02.017.

[50] Y.X. Tian, H.L. Cao, Y.Q. Qiao, F.H. Meng, X.Y. Liu, Antibacterial activity and cytocompatibility of titanium oxide coating modified by iron ion implantation, Acta Biomater. 10 (10) (2014) 4505–4517, https://doi.org/10.1016/j.actbio.2014.06.002.

[51] L. Yu, G.D. Jin, L.P. Ouyang, D.H. Wang, Y.Q. Qiao, X.Y. Liu, Antibacterial activity, osteogenic and angiogenic behaviors of copper-bearing titanium synthesized by PIII&D, J. Mater. Chem. B 4 (7) (2016) 1296–1309, https://doi.org/10.1039/C5TB02300A.

[52] K. Li, C. Sun, Z.Q. Chen, H.X. Qu, H.F. Xie, Q. Zhong, Fe-carbon dots enhance the photocatalytic nitrogen fixation activity of TiO$_2$@CN heterojunction, Chem. Eng. J. 429 (2022), https://doi.org/10.1016/j.cej.2021.132440.

[53] X. Tang, A.W. Yu, Q.Q. Yang, H.Y. Yuan, Z.H. Wang, J.Z. Xie, L.H. Zhou, Y. Guo, D. Ma, S. Dai, Significance of epitaxial growth of PtO$_2$ on rutile TiO$_2$ for Pt/TiO$_2$ catalysts, J. Am. Chem. Soc. 146 (6) (2024) 3764–3772, https://doi.org/10.1021/jacs.3c10659.

[54] L. Liu, J. Hu, X.Q. Fan, Y. Zhang, S.F. Zhang, B.T. Tang, Phase change materials with Fe$_3$O$_4$/GO three-dimensional network structure for acoustic-thermal energy

conversion and management, Chem. Eng. J. 426 (2021), https://doi.org/10.1016/j.cej.2021.130789.

[55] W. Guan, L. Tan, X.M. Liu, Z.D. Cui, Y.F. Zheng, K.W.K. Yeung, D. Zheng, Y. Q. Liang, Z.Y. Li, S.L. Zhu, X.B. Wang, S.L. Wu, Ultrasonic interfacial engineering of red phosphorous-metal for eradicating MRSA infection effectively, Adv. Mater. 33 (5) (2021), https://doi.org/10.1002/adma.202006047.

[56] Y.N. Liu, C.L. Miao, P.F. Yang, Y.F. He, J.T. Feng, D.Q. Li, Synergetic promotional effect of oxygen vacancy-rich ultrathin TiO$_2$ and photochemical induced highly dispersed Pt for photoreduction of CO$_2$ with H$_2$O, Appl. Catal. B Environ. 244 (2019) 919–930, https://doi.org/10.1016/j.apcatb.2018.12.028.

[57] G. Jia, Y. Wang, X. Cui, H. Zhang, J. Zhao, L.H. Li, L. Gu, Q. Zhang, L. Zheng, J. Wu, Q. Wu, D.J. Singh, W. Li, L. Zhang, W. Zheng, Wet-chemistry hydrogen doped TiO2 with switchable defects control for photocatalytic hydrogen evolution, Matter 5 (1) (2022) 206–218.

[58] X. Chen, L. Liu, P.Y. Yu, S.S. Mao, Increasing solar absorption for photocatalysis with black hydrogenated titanium dioxide nanocrystals, Science 331 (6018) (2011) 746–750, https://doi.org/10.1126/science.1200448.

[59] C.A. Zhou, K. Ma, Z. Zhuang, M. Ran, G. Shu, C. Wang, L. Song, L. Zheng, H. Yue, D. Wang, Tuning the local environment of Pt species at CNT@MO(2-x) (M = Sn and Ce) heterointerfaces for boosted alkaline hydrogen evolution, J. Am. Chem. Soc. 146 (31) (2024) 21453–21465, https://doi.org/10.1021/jacs.4c04189.

[60] A. Attaeyan, M. Shahgholi, A. Khandan, Fabrication and characterization of novel 3D porous titanium-6Al-4V scaffold for orthopedic application using selective laser melting technique, Iranian J. Chem. Chem. Eng. Int. English Edition 43 (1) (2024) 66–82.